

# Topological Chiral and Nematic Superconductivity by Doping Mott Insulators on Triangular Lattice

Yixuan Huang<sup>1</sup> and D. N. Sheng<sup>1,\*</sup>

<sup>1</sup>*Department of Physics and Astronomy, California State University, Northridge, California 91330, USA*

(Dated: July 18, 2022)

The mechanism of the unconventional topological superconductivity (TSC) remains a long-standing issue. We investigate the quantum phase diagram of the extended  $t$ - $J$ - $J_\chi$  model including spin chiral interactions on triangular lattice based on the state-of-the-art density matrix renormalization group simulations. We identify distinct classes of superconducting phases characterized by nonzero topological Chern numbers  $C = 1$  and  $2$ , and a nematic  $d$ -wave superconducting phase with a zero Chern number. The TSC states are shown to emerge from doping either a magnetic insulator or chiral spin liquid, which opens new opportunities for experimental discovery. In addition, we further classify the  $C = 2$  class of TSC phases into an isotropic and a nematic TSC phases, and present evidence of continuous quantum phase transitions from the nematic TSC phase to both isotropic TSC and nematic  $d$ -wave phases. These results provide new insight into the mechanism of TSC with an emphasis on the role played by hole dynamics, which changes spin background and drives a topological phase transition at a hole doping level around 3% upon doping a magnetic insulator to enable the emergence of the TSC.

## I. INTRODUCTION

There have been intensive studies of the canonical models for strongly correlated systems, the two-dimensional (2D) Hubbard and  $t$ - $J$  models, and their generalized versions since the discovery of high- $T_c$  cuprate superconductivity (SC) [1–7]. At the strong coupling limit, these models host different Mott insulating states varying from magnetic insulators to spin liquids [8]. Understanding the interplay of conventional orders, spin liquid physics and unconventional SC in doped Mott insulators is one of the central challenges of condensed matter physics. A large body of work on unconventional SC is connected to the original proposal of the resonating valence bond theory [1] that doping Mott insulators might naturally lead to SC [2, 5, 6, 9–11]. Lacking well-controlled analytical solutions in 2D with strong couplings, unbiased numerical studies play an important role in establishing the quantum phases in such models. Along this direction, exciting progress has been made in understanding the emergence of SC and its interplay with spin fluctuations and charge stripes by doping the antiferromagnetic Mott state on the square lattice based on extensive numerical simulations [12–23], which is relevant to cuprate SC. In particular, more recent density matrix renormalization group (DMRG) [24] studies have established robust SC for extended  $t$ - $J$  and Hubbard models on square lattice with next-nearest-neighbor hoppings suggesting the importance of tuning hole dynamics to enhance SC [15, 21–23].

Mott insulating states on triangular lattice offer another exciting playground and challenges for their distinct interplay between geometric frustrations, lattice rotational symmetry, and quantum fluctuations [7, 11, 25–

40]. On the experimental side, the SC state observed in  $\text{Na}_x\text{CoO}_2\cdot y\text{H}_2\text{O}$  might be a  $d + id$ -wave topological superconductivity (TSC) state which breaks time-reversal symmetry [41, 42]. More recently, different twisted transition metal dichalcogenide (TMD) moiré systems have been discovered to be quantum simulators of the Hubbard model [43, 44], which are promising systems hosting correlated insulators and topological superconductors [45–47].

Theoretically, the Kalmeyer-Laughlin (KL) chiral spin liquid (CSL) [48, 49] has been identified among the phase boundaries of different competing magnetic ordered states [50–54] for frustrated spin systems or near the Mott transition for the Hubbard model [36, 37] on triangular lattice. Whether doping a KL CSL can generally lead to the TSC [11, 32, 34, 48, 49, 55–57] remains an open question. A recent theoretical study [11] suggests that doping a KL CSL may naturally lead to a chiral metal while a topological  $d + id$ -wave SC represents a more nontrivial scenario requiring the internal gauge flux to be adjusted with the hole doping level. Indeed, unbiased numerical simulations have found a possible chiral metal by doping the CSL identified at half filling of the triangular Hubbard model [34, 36]. The nontrivial example of identifying the topological  $d + id$ -wave SC by doping the KL CSL comes from the study of the  $t$ - $J$ - $J_\chi$  model [32] with strong three-spin chiral interactions. The topological class of the observed TSC state [32] characterized by a finite integer quantized spin Chern number [58, 59] and chiral Majorana edge modes has not been revealed. Crucially, the driving mechanism for the emergence of the TSC remains to be identified, which may require extensive exploration in the parameter space by tuning relevant hopping parameters and interactions [32, 53, 54]. Given the fact that CSLs often emerge near the boundaries between different magnetically ordered states [53, 54], related open questions naturally arise including what the interplay is between

\* donna.sheng1@csun.edu

the TSC and conventional orders or fluctuations, and whether distinct unconventional SC states can emerge by doping different magnetically ordered states.

To address these open issues, we study the quantum phase diagram and focus on the emergent unconventional SC in the extended  $t$ - $J$ - $J_\chi$  model on triangular lattice based on large-scale DMRG simulations [24]. By tuning the ratios of the next-nearest- and nearest-neighbor hoppings ( $t_2/t_1$ ) and Heisenberg spin couplings ( $J_2/J_1$ ) in the presence of three spin chiral interactions ( $J_\chi$ ) [32], we identify different superconducting phases including distinct  $d + id$ -wave TSC phases that are characterized by nonzero topological Chern numbers  $C = 1$  and 2, and a nematic SC phase with a d-wave pairing symmetry breaking lattice rotational symmetry and  $C = 0$ . Furthermore, for weaker  $J_\chi$  the  $C=2$  phases include isotropic and nematic TSC phases with a continuous quantum phase transition between them. We demonstrate that these topological and nematic d-wave SC states have robust power-law decaying pairing correlations in the form of Luther-Emery liquid [60] on wider cylinders, which may lead to different superconducting states in 2D. The TSC can be induced by either doping a magnetically ordered state or CSL, which provides a new opportunity for experimental discovery of unconventional TSC. We also demonstrate the important role played by hole dynamics, which can drive a topological phase transition upon doping a  $120^\circ$  antiferromagnetic (AFM) state at a hole doping level  $\delta \approx 3\%$ , enabling the TSC to emerge. Furthermore, the nematic SC with  $C = 0$  can emerge from either doping the CSL or magnetic ordered states [53], suggesting the rich interplay between unconventional SC and spin background.

The rest of the paper is organized as follows. In Sec. II, we introduce the extended  $t$ - $J$ - $J_\chi$  model on a triangle lattice, the DMRG method, and the topological characterization for the SC states through spin flux insertion. Its quantum phase diagram is presented in Sec. III, containing different TSC phases and a nematic d-wave SC phase. We demonstrate their distinct topological Chern numbers (Sec. III A), the quasi-long-range order in SC pairing correlations (Sec. III B), and the pairing symmetries (Sec. III C) to characterize these phases. In Sec. IV we focus on the quantum phase transitions by tuning the ratios of  $t_2/t_1$  and  $J_2/J_1$ , with Sec. IV A showing the evolution of SC pairing correlations, Sec. IV B addressing the nature of quantum phase transitions among different phases, and Sec. IV C showing the evolution of spin correlations. The summary and discussions are presented in Sec. V.

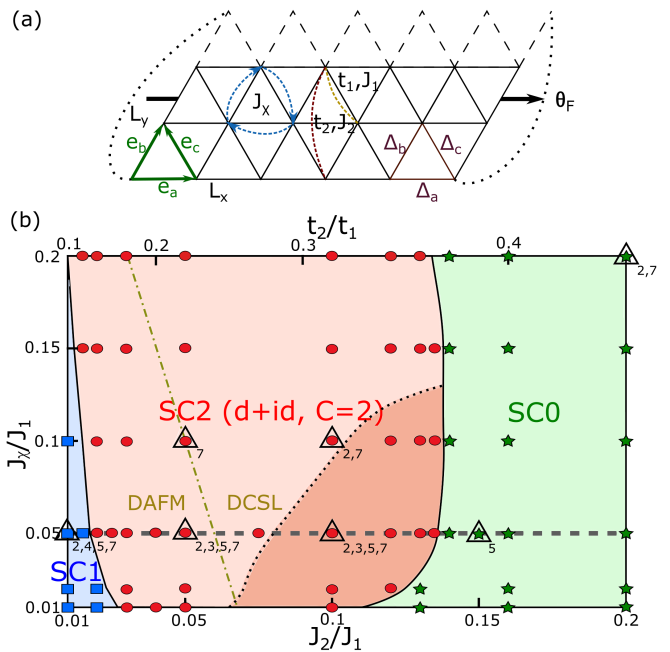


FIG. 1. Quantum phase diagram. (a) Schematic illustration of the extended  $t$ - $J$ - $J_\chi$  model on triangle lattice with the nearest-neighbor and the next-nearest-neighbor hoppings  $t_1$  and  $t_2$  and Heisenberg exchange  $J_1$  and  $J_2$  interactions, as well as the three-spin chiral interactions  $J_\chi$ . The dashed lines indicate the periodic boundary condition. (b) The quantum phase diagram obtained on  $L_y = 6$  cylinders based on the Chern number simulations. For  $0.01 \leq J_2/J_1, J_\chi/J_1 \leq 0.2$  and doping level  $\delta = 1/12$ , we identify distinct classes of SC phases labeled as SC1, SC2, and SC0 from left to right characterized by their spin Chern number  $C$ . The SC2 regime represents two phases, the isotropic TSC (lighter red region) and nematic TSC (darker red region) phases. Different symbols represent parameter points studied with the DMRG methods. The triangles mark points presented in the paper with the lower indices representing the indices of figures. A scan of the Chern number, SC pairing symmetry and energy/entropy along the horizontal dashed line is used in Figs. 2(c), 5(d), and 6, respectively. The main feature of the phase diagram is essentially the same for other doping levels  $\delta = 1/24 - 1/8$ .

## II. MODEL AND METHOD

We study the extended  $t$ - $J$ - $J_\chi$  model that is defined as

$$\begin{aligned}
 H = & - \sum_{\{ij\},\sigma} t_{ij} (\hat{c}_{i,\sigma}^\dagger \hat{c}_{j,\sigma} + H.c.) + \sum_{\{ij\}} J_{ij} (\hat{\mathbf{S}}_i \cdot \hat{\mathbf{S}}_j - \frac{1}{4} \hat{n}_i \hat{n}_j) \\
 & + J_\chi \sum_{\{ijk\} \in \nabla/\Delta} \hat{\mathbf{S}}_i \cdot (\hat{\mathbf{S}}_j \times \hat{\mathbf{S}}_k), \quad (1)
 \end{aligned}$$

where  $\hat{c}_{i,\sigma}^\dagger$  is the electron creation operator on site  $i$  with spin index  $\sigma = \pm 1$ ,  $\hat{\mathbf{S}}_i$  is the spin- $\frac{1}{2}$  operator and  $\hat{n}_i = \sum_\sigma \hat{c}_{i,\sigma}^\dagger \hat{c}_{i,\sigma}$  is the electron number operator. We consider the nearest-neighbor and the next-nearest-neighbor hoppings  $t_1$  and  $t_2$  as well as Heisenberg couplings  $J_1$  and  $J_2$ , supplemented by the three-spin chi-

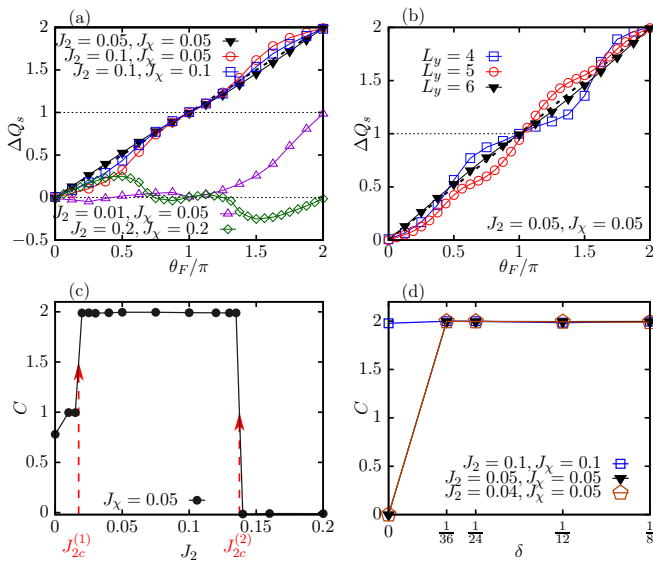


FIG. 2. The pumped spin by inserting flux and spin Chern number. (a) The pumped spin  $\Delta Q_s$  with adiabatically inserted flux  $\theta_F$  is shown for different SC phases on the  $L_y = 6$  cylinder. For the three parameter points in the SC2 phase the measured spin pumping after inserting one flux quantum  $\Delta Q_s|_0^{2\pi} = 1.993, 1.983, 1.990$ , respectively, indicating that the error bar is around 1% from the exactly quantized value  $\Delta Q_s|_0^{2\pi} = 2$  for different systems. (b)  $\Delta Q_s$  versus  $\theta_F$  for  $J_2 = J_\chi = 0.05$  inside SC2 phase on  $L_y = 4, 5, 6$  cylinders. (c) The evolution of Chern number  $C$  with varying  $J_2$  at  $J_\chi = 0.05$  on  $L_y = 6$ .  $C = \Delta Q_s|_0^{2\pi}$  is obtained after inserting one flux quantum  $\theta_F = 0 \rightarrow 2\pi$ . SC1-SC2 and SC2-SC0 phase transitions take place at  $J_2 = J_{2c}^{(1)}, J_{2c}^{(2)}$ , respectively, where the Chern number jumps. The doping level is  $\delta = 1/12$  for (a)-(c). (d)  $C$  versus  $\delta$  for parameter points with different undoped parent states (e.g. DAFM or DCSL) on  $L_y = 6$ .

ral interactions  $J_\chi$  on every elementary triangle as illustrated in Fig. 1(a). The chiral interaction can be generated from the Hubbard model with an external magnetic field [32]. We set  $J_1 = 1$  as the unit of energy,  $t_1 = 3$ ,  $J_2/J_1 = (t_2/t_1)^2$ , and focus on the regime of  $0 < J_2, J_\chi \leq 0.2$  with hole doping level  $\delta \leq 1/8$ , which is the optimal doping region for unconventional SC [22, 32].

To obtain the ground state of the Hamiltonian in Eq. (1), we apply the DMRG method with  $U(1) \times SU(2)$  for charge and spin symmetries [61] on cylinder systems with an open boundary condition along the axis ( $e_a$  or  $x$ -) direction and a periodic boundary condition along the circumferential ( $e_b$  or  $y$ -) direction, as illustrated in Fig. 1(a). The number of sites is  $N = L_x \times L_y$  where  $L_x$  and  $L_y$  denote the lengths in these two directions, respectively. The number of electrons  $N_e$  is related to the doping level  $N_e/N = 1 - \delta$ . We keep up to  $M = 12000$   $SU(2)$  spin multiplets [equivalent to about  $m = 36000$   $U(1)$  states] with truncation error  $\epsilon \sim 10^{-6}$ , which leads to accurate results (see Supplemental Sec. II [62] for details). We develop a topological characterization for the SC states through the spin flux insertion by adiabati-

cally evolving the ground state as a function of a twisted boundary phase  $\theta_F$  based on the method established for CSL and fractional quantum Hall systems [52, 63]. The flux adds a spin-dependent phase factor to the electron hoppings  $\hat{c}_{i,\sigma}^\dagger \hat{c}_{j,\sigma} \rightarrow e^{i\sigma\theta_F} \hat{c}_{i,\sigma}^\dagger \hat{c}_{j,\sigma}$  if  $j \rightarrow i$  crossing the  $y$  boundary from the top (see Fig. 1(a)), and similarly couples to the spin flip terms [52]. In this type of calculation,  $SU(2)$  symmetry is broken by the spin flux and we use  $U(1) \times U(1)$  symmetries with bond dimensions up to  $m = 8000$  for accurate results due to the robustness of the topologically protected spin pumping (see Supplemental Sec. I [62] for more details).

### III. QUANTUM PHASE DIAGRAM

At half filling (with no doping  $\delta = 0$ ), the Hamiltonian in Eq. (1) reduces to the Heisenberg  $J_1$ - $J_2$ - $J_\chi$  model [53]. In the small  $J_2$  regime ( $J_1 = 1$ ), the  $120^\circ$  AFM order survives up to  $J_2 \approx 0.07$  at  $J_\chi = 0$ , which smoothly extends to the nonzero  $J_\chi$  regime. The intermediate  $J_2$  regime is dominated by the CSL, which separates from the AFM order by the dash-dotted line as shown in Fig. 1(b) obtained from Refs. [53, 54]. Through extensive DMRG simulations of topological Chern numbers and SC pairing correlations on  $L_y = 4$ -6 cylinders for hole-doped systems, we establish a quantum phase diagram in the parameter space  $0 < J_2, J_\chi \leq 0.2$  for doping  $\delta = 1/12$ , with three distinct classes of superconducting phases stabilized by small  $J_2, J_\chi \geq 0.01$  [64] as shown in Fig. 1(b). These SC phases are characterized by different topological spin Chern numbers. At small  $J_2$  we find a topological chiral  $d + id$ -wave SC phase with spin Chern number  $C = 1$  (labeled as SC1) by doping the AFM (DAFM) state. In the intermediate  $J_2$  regime, another class of topological  $d + id$ -wave SC phases emerges characterized by a quantized  $C = 2$  (SC2), which can be induced by doping either the AFM state or the CSL (DCSL) as illustrated in Fig. 1(b). The SC2 class is further divided into an isotropic TSC phase and a nematic TSC phase breaking rotational symmetry. Interestingly, the nematic TSC state is an analog state of the recently revealed nematic fractional quantum Hall effect [65–68]. At larger  $J_2$ , the SC phase has a  $d$ -wave symmetry with anisotropic pairing correlations breaking the lattice rotational symmetry and  $C = 0$  (SC0) indicating a topologically-trivial SC phase. The SC0 phase belongs to the same quantum phase as the nematic  $d$ -wave SC identified for an extended  $t$ - $J$  model [33] with time-reversal symmetry. The phase diagram is essentially the same for other doping levels  $\delta = 1/24$ - $1/8$  with small shifts in phase boundaries (e.g., at  $\delta = 1/8$ ,  $\Delta J_{2c}^{(1)} \approx 0.01 \sim 0.02$  where  $J_{2c}^{(1)}$  denotes the critical  $J_2$  between SC1 and SC2). We also find that the previously revealed  $d + id$ -wave SC state (at  $J_\chi = 0.4$  and  $J_2 = t_2 = 0.0$ ) [32] has  $C = 2$  sitting near the phase boundary of the SC2 phase.

### A. Topological Chern number characterization through flux insertion

The nonzero Chern number characterizes the topological nature of the  $d + id$ -wave superconductors [58, 59], which also identifies the number of chiral Majorana edge modes. We determine the spin Chern number through the spin pumping with inserting flux  $\theta_F$  into the cylinder, as illustrated in Fig. 1(a). The net spin with nonzero  $S_z$  accumulates near the boundaries of the cylinder as the flux adiabatically increases, while the total  $S_z = 0$  for the ground state at different  $\theta_F$ . We use a small step for the increase of the flux  $\theta_F \rightarrow \theta_F + \Delta\theta_F$  with  $\Delta\theta_F = 2\pi/16$ . A finite Chern number [52] can be obtained from the total spin pumping  $C = \Delta Q_s|_0^{2\pi} = (n_\uparrow - n_\downarrow)_0^{2\pi}$  measured at the left boundary at  $\theta_F = 0$  and  $2\pi$ , where  $n_\sigma$  is the accumulated charge near the boundary with spin  $\sigma$ . We directly measure the pumped spin for each  $\theta_F$  from the reduced density matrix by calculating the sum  $Q_s = \sum_\alpha \lambda_\alpha (n_{\uparrow,\alpha} - n_{\downarrow,\alpha})$ , where  $\lambda_\alpha$  is the eigenvalue and  $\alpha$  the eigenstate of the reduced density matrix [63], and  $n_{\uparrow,\alpha}$  ( $n_{\downarrow,\alpha}$ ) is the particle number of the  $\alpha$  state with up (down) spin. Because the inserted flux breaks SU(2) symmetry, we use infinite DMRG with U(1)×U(1) symmetries with a large unit cell that is commensurate with the doping level (see Supplemental Sec. I [62]).

We show examples of the flux insertion and the resulting Chern numbers for systems with  $\delta = 1/12$  in Fig. 2(a). For three parameter points inside the SC2 phase on the  $L_y = 6$  system, the  $\Delta Q_s$  increases almost linearly with  $\theta_F$  indicating uniform Berry curvature [69], and there is  $\Delta Q_s \approx 2.0$  net spin pumped to the boundary after the threading of one flux quantum ( $\theta_F = 0 \rightarrow 2\pi$ ). This corresponds to the quantized Chern number  $C = 2$ , which remains the same on various  $L_y = 4, 5,$  and  $6$  as shown in Fig. 2(b). The pumping rate becomes more uniform with the increase of  $L_y$ , indicating the increased robustness of the topological quantization for larger systems. In contrast, at  $J_2 = 0.01, J_\chi = 0.05$  inside the SC1 phase, we find no linear relation between  $\Delta Q_s$  and  $\theta_F$  which indicates the nonuniform Berry curvature versus boundary phase  $\theta_F$  [69]. The measured  $\Delta Q_s \approx 0.983$ , indicating around one net spin pumped with the insertion of one flux quantum and  $C = 1$ . The Chern number becomes nonquantized extended to the  $J_2 = 0$  limit as shown in Fig. 2(c) signaling gapless low-energy excitations. We believe the large variance of the Berry curvature versus  $\theta_F$  for the SC1 phase may indicate a topological state with gapless excitations at small  $J_2$  consistent with an early proposal for a topological superconducting state for the  $\text{Na}_x\text{CoO}_2 \cdot y\text{H}_2\text{O}$  system based on variational simulations [42]. In the SC0 phase at larger  $J_2 = J_\chi = 0.2$ , we find  $\Delta Q_s \approx -0.01$  which confirms  $C = 0$  for a topologically trivial SC state. Thus, the phase transitions between the three phases can be characterized by jumps of topological Chern number  $C$  with varying  $J_2$  at a fixed  $J_\chi = 0.05$  as illustrated in Fig. 2(c).

Since the undoped ( $\delta = 0$ ) parent state of the SC2

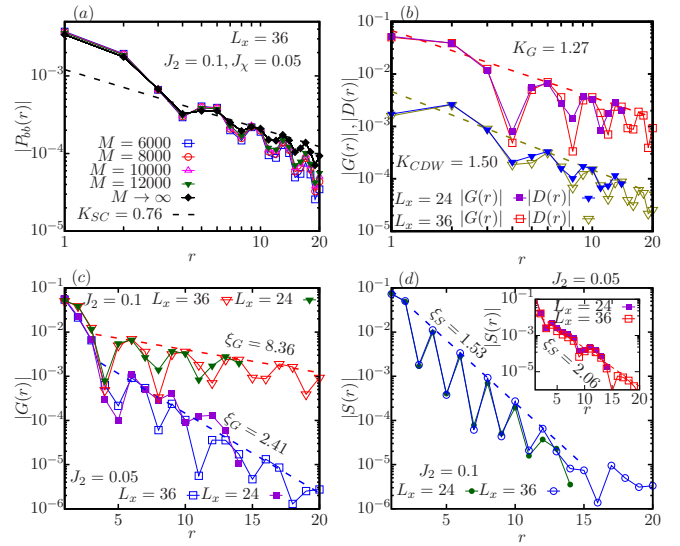


FIG. 3. Pairing and other correlations in SC2. (a) The SC pairing correlations for different bond dimensions  $M$  at  $J_2 = 0.1, J_\chi = 0.05$  for  $N = 36 \times 6$  system.  $\mathbf{r}$  is chosen along the  $x$  direction  $\mathbf{r} = (r, 0)$  and the reference point is  $\mathbf{r}_0 = (L_x/4, y_0)$  to avoid the boundary effect (the results are independent of  $y_0$  because of the translational invariance along the  $y$  direction). The straight-line fit in the log-log plot of the extrapolated data in the infinite  $M$  limit follows a power-law behavior. (b) The density-density correlation  $|D(r)|$  and single-particle correlation  $|G(r)|$  which are fit by the power-law relation for  $N = 24 \times 6$  and  $36 \times 6$ , at  $J_2 = 0.1, J_\chi = 0.05$ . (c) The comparison of  $|G(r)|$  at  $J_2 = 0.05$  and  $0.1$  with the same  $J_\chi = 0.05$ , which demonstrates the fast growing of the correlation length  $\xi_G$  with the increase of  $J_2$ . (d) The exponential decay of the spin correlations  $|S(r)|$  in the main figure and its inset for the same parameters as in (c), where  $r > 15$  data points are ignored in the fitting because their values are comparable to the numerical truncation error. The doping level is  $\delta = 1/12$ . The obtained fitting exponents or correlation lengths have error bars around 0.02, except for the one in the inset of (d) which is around 0.06.

phase contains both the AFM state and CSL, a natural question is how the Chern number evolves with the doping level. As demonstrated in Fig. 2(d), for two points in the DAFM regime at  $J_2 = 0.04, 0.05$  and  $J_\chi = 0.05$ ,  $C$  jumps from 0 to 2 at a small doping of  $\delta = 1/36$  and remains quantized at  $C = 2$  for larger  $\delta$ , which demonstrates a doping-induced topological quantum phase transition. On the contrary, in the DCSL regime at  $J_2 = J_\chi = 0.1$ ,  $C = 2$  for  $\delta = 0-1/8$  which shows a robust Chern number quantization from the parent CSL to the topological  $d + id$ -wave SC. This is consistent with the fact that the KL CSL is a bosonic  $\nu = 1/2$  fractional quantum Hall state [48, 49, 58], which is equivalent to the  $C = 2$  topological order for fermionic systems where the phase space is enlarged by a factor of 4 in the definition of the Chern number [70] with a doubled flux period for the Hamiltonian to be invariant. The ex-

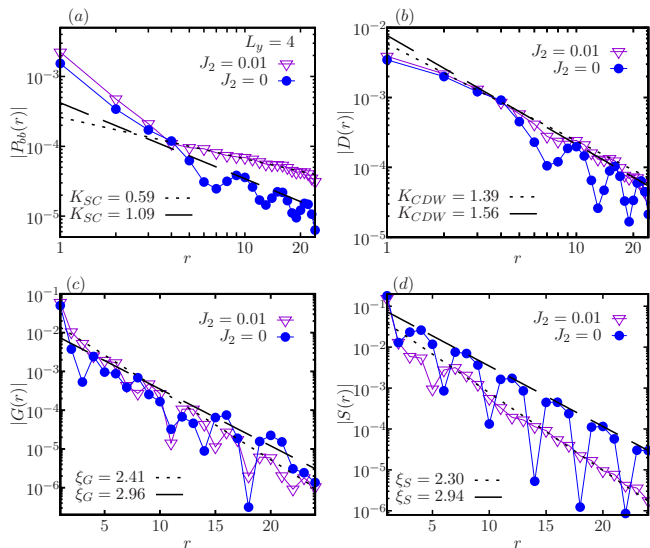


FIG. 4. Pairing and other correlations at  $J_x = 0.05$  for smaller  $J_2$  on  $L_y = 4$ . The results are converged with a large bond dimension  $M = 10000$ . (a) The SC pairing correlations.  $\mathbf{r}$  is chosen along x-direction  $\mathbf{r} = (r, 0)$  and the reference point is  $\mathbf{r}_0 = (L_x/4, L_y/2)$  to avoid the boundary effect. The straight-line fit in the log-log plot follows a power-law behavior, with exponents of 1.09 and 0.59 for  $J_2 = 0$  and 0.01, respectively. (b) The density-density correlations  $|D(r)|$  which are fit by a power-law relation, with exponents of 1.56 and 1.39 for  $J_2 = 0$  and 0.01, respectively. (c) The single particle correlations  $|G(r)|$  which are fit by an exponential decay with correlation lengths of 2.96 and 2.41 for  $J_2 = 0$  and 0.01, respectively. (d) The spin correlations  $|S(r)|$  which are fit by an exponential decay with correlation lengths of 2.94 and 2.30 for  $J_2 = 0$  and 0.01, respectively. The doping level is  $\delta = 1/12$ . The obtained fitting exponents or correlation lengths have error bars around 0.03.

act quantization  $C = 2$  of the SC2 phase indicates that doped holes can indeed adjust the internal flux with the hole doping level to realize a bosonic integer quantum Hall effect for holons [11].

### B. Quasi-long-range order in superconducting pairing correlations

To explore the superconducting nature of the system, we focus on the dominant spin singlet pairing correlations  $P_{\alpha\beta}(\mathbf{r}) = \langle \hat{\Delta}_\alpha^\dagger(\mathbf{r}_0) \hat{\Delta}_\beta(\mathbf{r}_0 + \mathbf{r}) \rangle$ , where the pairing operator  $\hat{\Delta}_\alpha(\mathbf{r}) = (\hat{c}_{\mathbf{r}\uparrow} \hat{c}_{\mathbf{r}+e_{\alpha\downarrow}} - \hat{c}_{\mathbf{r}\downarrow} \hat{c}_{\mathbf{r}+e_{\alpha\uparrow}}) / \sqrt{2}$  with  $\alpha = a, b, c$ , representing different nearest-neighboring bonds as illustrated in Fig. 1(a).

We first give an example of the SC pairing correlations in the SC2 regime as shown in Fig. 3(a), where the magnitude of pairing correlations at longer distance for two  $b$  bonds (along the  $y$  direction)  $|P_{bb}(r)|$  increases gradually as the DMRG bond dimension increases from  $M = 6000$  to 12000 at  $J_2 = 0.1, J_x = 0.05$  on  $N = 36 \times 6$  system.

Because the DMRG represents the ground state in the matrix product form [71] with finite bond dimensions, the scaling to  $M \rightarrow \infty$  is needed to identify the true nature of long-distance correlations for wider cylinders. Using a second-order polynomial fitting of  $1/M$ , we find that the extrapolated  $|P_{bb}(r)|$  shows a power-law decay with distance  $|P_{bb}(r)| \sim r^{-K_{SC}}$ , with the Luttinger exponent  $K_{SC} \approx 0.76$ . Similar results are obtained for correlations with other bonds, and also for different  $L_x$  or  $L_y = 4$  systems (see Supplemental Sec. III. A [62]).  $K_{SC} \lesssim 1$  holds for SC2 phase, indicating a strong divergent SC susceptibility in the zero-temperature limit [33].

We then turn to the density-density  $D(\mathbf{r}) = \langle \hat{n}_{\mathbf{r}_0} \hat{n}_{\mathbf{r}_0 + \mathbf{r}} \rangle - \langle \hat{n}_{\mathbf{r}_0} \rangle \langle \hat{n}_{\mathbf{r}_0 + \mathbf{r}} \rangle$  and single-particle  $G(\mathbf{r}) = \sum_\sigma \langle \hat{c}_{\mathbf{r}_0, \sigma}^\dagger \hat{c}_{\mathbf{r}_0 + \mathbf{r}, \sigma} \rangle$  correlations. As shown in Fig. 3(b), the  $|D(r)|$  decays with a power-law relation at long distance using extrapolated data. The Luttinger exponent for density-density correlations is  $K_{CDW} \approx 1.50$  much larger than  $K_{SC}$ . Both  $|P_{bb}(r)|$  and  $|D(r)|$  show similar spatial oscillations consistent with the electron density oscillation in real space (see Supplemental Sec. V [62]). Similarly, the single-particle Green function  $|G(r)|$  can also be fit into power-law behavior [Fig. 3(b)]. Interestingly, we identify a crossover for  $|G(r)|$  with the increase of  $J_2$ . At smaller  $J_2 = 0.05$  in the SC2 regime, we observe an exponential decay in  $|G(r)|$  with a short correlation length  $\xi_G \approx 2.41$  which is consistent with the gapped isotropic TSC state as shown in Fig. 3(c). With the increase of  $J_2$ , the correlation length for  $|G(r)|$  increases to  $\xi_G \approx 8.36$  larger than  $L_y$ , which could also be fitted by a power-law decay [as shown in Fig. 3(b)] at  $J_2 = 0.1$  for fixed  $J_x = 0.05$  on different systems  $N = 24 \times 6$  and  $36 \times 6$ . The evolution of the single-particle correlation length is a signature of the evolution of the quasiparticle excitation gap, which gradually reduces with the increase of the  $J_2$  approaching the quantum phase transition from gapped SC state to a nodal nematic SC state as we will address further in Sec. IV. In comparison, the spin-spin correlations remain exponentially decay with a short correlation length  $\xi_S \approx 1.53$  (2.06) as shown in the main panel (inset) in Fig. 3(d) at  $J_2 = 0.1$  (0.05), indicating a finite spin gap which protects the SC state. These results provide compelling evidence for the robust SC pairing correlations as dominant correlations for SC phases with  $C = 2$ , which are the quasi-1D descendent states of 2D topological superconductors.

Now we discuss the features of various correlations at small  $J_2$ , where the SC1 phase is identified with the Chern number  $C = 1$ . The SC pairing correlations are shown in Fig. 4(a), where the magnitude of the SC pairing correlations  $|P_{bb}(r)|$  show power-law behavior with the Luttinger exponents  $K_{SC} \approx 1.09$  and 0.59 for  $J_2 = 0$  and 0.01, respectively, obtained with a fixed  $J_x = 0.05$  for  $N = 48 \times 4$  system. In comparison, as shown in Fig. 4(b), the  $|D(r)|$  decays with a power-law relation with larger exponents ( $K_{CDW} \approx 1.56$  and 1.39), while the  $|G(r)|$  (Fig. 4(c)) and  $|S(r)|$  (Fig. 4(d)) both decay exponen-

tially with small correlation lengths. These results indicate that SC1 phase has dominant SC correlations observed for  $L_y = 4$  cylinders. We also confirm power-law SC correlations for a wider system of  $N = 20 \times 6$  at  $J_2 = 0.01, J_\chi = 0.05$  with good numerical convergence for this possible gapless phase. Interestingly, there are stronger spin correlations for the  $L_y = 6$  system indicating a vanishing or very small spin gap (see Supplemental Sec. III. D [62]), which is consistent with the fact that the SC1 phase has a spin gap-closing transition from  $C = 2$  phase.

We further confirm that the SC0 phase has robust quasi-long-range SC pairing correlations with a Luttinger exponent  $K_{SC} \approx 1.10$  at  $J_2 = J_\chi = 0.2$  dominating the density-density correlations. This phase can be smoothly connected to the d-wave phase identified by doping the  $J_1$ - $J_2$  model [33] with larger  $J_2$  (see Supplemental Sec. III. C [62] for more details).

There are other competing quantum phases and additional quantum phase transitions as we reduce the three spin chiral interactions to zero in the small  $J_2$  regime. For example, at  $J_2 = J_\chi = 0$ , the ground state is dominated by charge stripe and spin fluctuations with suppressed pairing correlations. Furthermore, additional results for  $L_y = 4$  with small  $J_2$  for a possible pairing density wave SC phase [38], and a d-wave SC phase co-existing with phase separation are shown in the Supplemental Sec. III. F [62]. These results provide further support that a small but finite chiral interaction plays an important role in stabilizing the topological SC phases for the systems we have studied.

### C. Pairing symmetry for topological and nematic SC phases

The SC pairing symmetry can be identified by the phases of the pairing correlations for different bonds. To extract the phase we rewrite the SC pairing correlation as  $P_{\alpha\beta}(\mathbf{r}) = |P_{\alpha\beta}(\mathbf{r})| e^{i\phi_{\alpha\beta}(\mathbf{r})}$  where  $\phi_{\alpha\beta}(\mathbf{r})$  is the phase for the correlation, and the pairing order parameter as  $\Delta_\alpha(\mathbf{r}) = |\Delta_\alpha(\mathbf{r})| e^{i\theta_\alpha(\mathbf{r})}$ . Using the definition of the pairing correlations, we obtain  $\theta_{\alpha\beta}(\mathbf{r}) = \theta_\alpha(\mathbf{r}) - \theta_\beta(\mathbf{r}) = \phi_{\alpha\alpha}(\mathbf{r}) - \phi_{\alpha\beta}(\mathbf{r})$  as the relative phases of the pairing order parameters for different nearest-neighbor bonds; see illustrations in the inset in Fig. 5(a). The pairing symmetry for different SC states is illustrated in Fig. 5(a) on  $N = 36 \times 6$  systems. At  $J_2 = J_\chi = 0.05$  in the SC2 regime,  $\theta_{\alpha\beta}(r)$  remains almost independent of  $r$  and the phases for order parameters are nearly quantized to  $[\theta_{bb}, \theta_{bc}, \theta_{ba}] \approx [0, -0.64\pi, 0.65\pi] \approx [0, -\frac{2}{3}\pi, \frac{2}{3}\pi]$ , which represents an isotropic  $d + id$  wave with  $C_3$  rotational symmetry. The angles  $\theta_{ba}$  and  $\theta_{bc}$  are closer to  $\pm 2\pi/3$  on wider system  $L_y = 6$  compared with  $L_y = 4$  results (with  $L_x = 48$ ) as shown in Figs. 5(a) and 5(b). At larger  $J_2 = 0.15$  with  $J_\chi = 0.05$  in the SC0 phase, these phases become  $[\theta_{bb}, \theta_{bc}, \theta_{ba}] \approx [0, -0.93\pi, 0.93\pi] \approx [0, -\pi, \pi]$ , which are nearly independent of  $L_y = 4$  or 6, suggest-

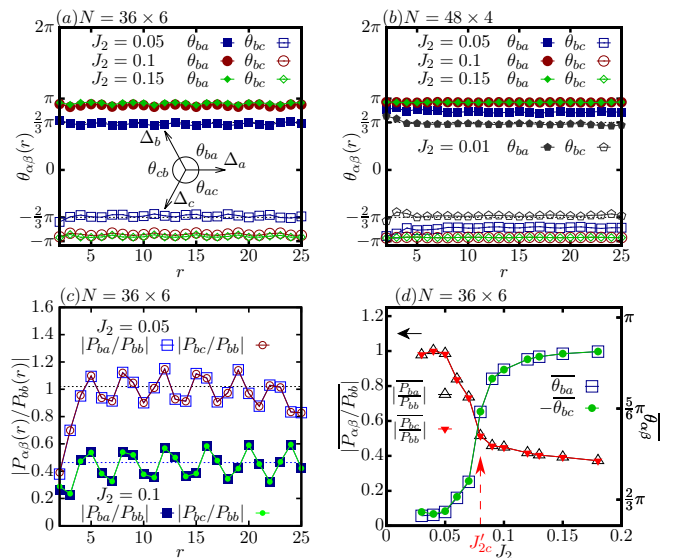


FIG. 5. Transition from the  $d + id$ -wave SC2 phases to SC0 phase. (a) The spatial dependence of relative phases for SC order parameters for various  $J_2$  on the  $L_y = 6$  ( $L_x = 36$ ) system.  $\mathbf{r}$  is chosen along the  $x$  direction  $\mathbf{r} = (r, 0)$ . (b) The relative phases for SC order parameters on the  $L_y = 4$  ( $L_x = 48$ ) system. (c) The ratio of the magnitudes of different SC correlations. The dashed line indicates the average over distances. (d) The spatial average values of the relative phases of SC order parameters and the ratios of magnitudes of different SC correlations for various  $J_2$ . All results are obtained at  $J_\chi = 0.05$  with bond dimension  $M = 10000$  ( $M = 8000$ ) on  $L_y = 6$  ( $L_y = 4$ ) systems. The doping level is  $\delta = 1/12$ .

ing a  $d$ -wave SC state consistent with the Chern number  $C = 0$  for this phase.

On the other hand, the relative strength of the SC correlations for different bonds also evolves with the increase of  $J_2$ . As shown in Fig. 5(c),  $|P_{ba}(r)/P_{bb}(r)|$  and  $|P_{bc}(r)/P_{bb}(r)|$  have spatial oscillations, and remain almost a constant average as  $r$  increases, which suggests a power-law-decaying behavior of  $|P_{ba}(r)|$  and  $|P_{bc}(r)|$  with the same exponents  $K_{SC}$ . At smaller  $J_2 = 0.05$ , the ratios  $|P_{ba}(r)/P_{bb}(r)|$  and  $|P_{bc}(r)/P_{bb}(r)|$  are close to 1.0, while they drop to around 0.46 observed at  $J_2 = 0.1$ , keeping the same  $J_\chi = 0.05$ . We further show an example of the SC1 phase at  $J_2 = 0.01$  and  $J_\chi = 0.05$  on  $L_y = 4$  in Fig. 5(b) with nearly quantized phases  $[\theta_{bb}, \theta_{bc}, \theta_{ba}] \approx [0, -0.64\pi, 0.64\pi] \approx [0, -\frac{2}{3}\pi, \frac{2}{3}\pi]$ . From mean-field theory, the isotropic SC1 state with  $C = 1$  has nodal quasiparticle excitations [42] and we leave the full nature of this state to future study due to the increased difficulty of converging the SC correlations for this critical phase on  $L_y = 6$ .

## IV. SYMMETRY EVOLUTION AND PHASE TRANSITIONS

### A. Evolution of the pairing order parameters

Now we focus on the symmetry evolution of the pairing order parameters from SC2 phases to SC0 phase. As shown in Fig. 5(d), the  $-\theta_{bc}$  and  $\theta_{ba}$  averaged over the middle 24 columns of the system with  $L_x = 36$  increase monotonically from  $\frac{2}{3}\pi$  towards  $\pi$  as  $J_2$  increases. At the same time, we find direct evidence of the increased nematicity as  $J_2$  increases, which is identified by the ratio of the magnitudes of SC pairing correlations for different bonds. As shown in Fig. 5(d), the spatial averaged ratios  $|P_{ba}/P_{bb}|$  and  $|P_{bc}/P_{bb}|$  decrease monotonically from 1 to around 0.4 at larger  $J_2$  side. A transition from an isotropic TSC phase to a nematic SC phase takes place inside the SC2 regime as indicated by the arrow in Fig. 5(d) pointing to a critical  $J'_{2c}$ , where both the  $|P_{ba}/P_{bb}|$  and  $|P_{bc}/P_{bb}|$  decrease quickly to the near saturated value. This feature revealed by the nematicity evolution shows a transition inside the SC2 regime, indicating that a nematic TSC phase emerges for  $J'_{2c} < J_2 < J_{2c}^{(2)}$ . As shown in Fig. 1(b), we identify a finite regime with increased nematicity in the SC pairing correlations while its topological nature remains the same with the Chern number  $C = 2$ , which is consistent with a nematic TSC state emerging within  $C = 2$  class of SC phases. The phase boundary is determined by the quick increase of  $\theta_{ba}$  to around  $\frac{5}{6}\pi$ . The emergent nematic TSC state is an analog state to the nematic fractional quantum Hall state with gapless collective excitations [65–68]. With further increase of  $J_2$ , the topological quantum phase transition takes place where the nematic  $d$ -wave SC state is recovered in the SC0 phase.

### B. Nature of quantum phase transitions

We now explore the nature of quantum phase transitions by following the energy and entanglement entropy evolution along the parameter line of  $J_\chi = 0.05$ . To calculate the entanglement entropy  $S$ , the cylinder is cut into two equal halves and  $S$  is obtained from the eigenvalues  $\lambda_i$  of the reduced density matrix  $S = -\sum_i \lambda_i \log(\lambda_i)$ . As shown in Fig. 6(a), the energy per site  $E_0$  shows a small kink and the entropy  $S$  shows a large jump at  $J_{2c}^{(1)} \approx 0.021$  which is very close to the transition point between  $C = 1$  and  $C = 2$  phase, indicating a first order transition between SC1 and the isotropic TSC (SC2) phase. The first order transition is further revealed by  $-dE_0/dJ_2$  given in Fig. 6(b), which shows discontinuity around  $J_{2c}^{(1)}$ . Two other transitions from the isotropic TSC to nematic TSC and from nematic TSC to  $d$ -wave SC are continuous transitions with smooth evolution of  $E_0$  and  $S$  (Fig. 6(a)), and their derivatives (Figs. 6(c) - (f)). Interestingly, the transition point between the

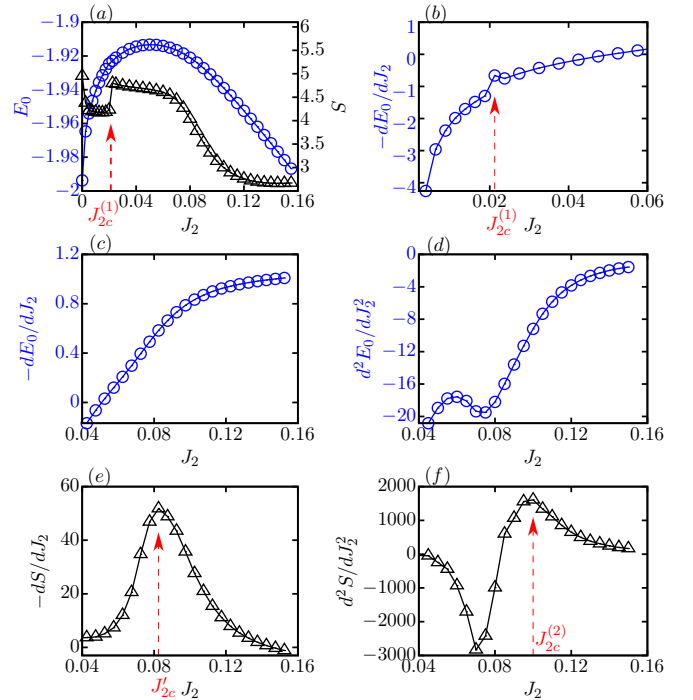


FIG. 6. The energy per site  $E_0$  and entanglement entropy  $S$  for various  $J_2$  obtained at fixed  $J_\chi = 0.05$  on a  $N = 16 \times 6$  cylinder. (a) The energy and entanglement entropy, where  $J_{2c}^{(1)}$  is identified from the small jump in  $S$ . (b) The first order derivative of  $E_0$  with respect to  $J_2$  where  $J_{2c}^{(1)}$  is identified at the discontinuity point. (c) The first order derivative of  $E_0$  for larger  $J_2$ . (d) The second order derivative of  $E_0$  for larger  $J_2$ . (e) The first order derivative of  $S$  where  $J_{2c}^{(2)}$  is identified as the peak. (f) The second order derivative of  $S$  where  $J_{2c}^{(2)}$  is identified as the peak. The results are obtained with  $M = 10000$ . The doping level is  $\delta = 1/12$ .

isotropic TSC to nematic TSC is indicated by the peak in  $-dS/dJ_2$ , which is very close to the one identified by the nematicity in SC pairing correlations. The transition between nematic TSC and the nematic  $d$ -wave SC may be identified by the peak in  $d^2S/dJ_2^2$ , which is shifted from the one identified by the Chern number with flux insertion into a very long cylinder studied in the infinite DMRG. This may be explained by the finite size effect for identifying higher order transitions where the peaks in entropy usually shift with system lengths [72, 73].

### C. Evolution of the spin correlations

The evolution of spin correlations can be studied through the spin structure factor defined as  $S(\mathbf{k}) = \frac{1}{N'} \sum_{i,j} \langle \mathbf{S}_i \cdot \mathbf{S}_j \rangle e^{i\mathbf{k} \cdot (\mathbf{r}_i - \mathbf{r}_j)}$  for a system with  $N = 36 \times 6$ , where  $i$  and  $j$  are summed over the middle  $N' = 2L_y \times L_y$  sites to avoid boundary effects. As shown in Fig. 7(a),  $S(\mathbf{k})$  has strong peaks at the  $\mathbf{K}$  points representing strong  $120^\circ$  AFM fluctuations at short distances for

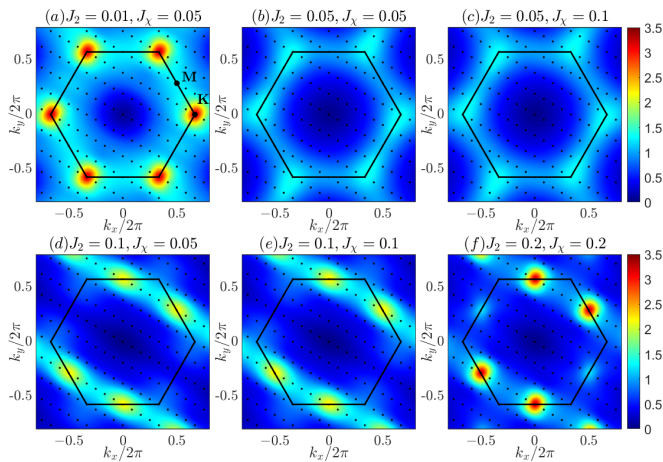


FIG. 7. The spin structure factor  $S(\mathbf{k})$  obtained on an  $N = 36 \times 6$  cylinder using correlations from middle  $N' = 12 \times 6$  sites. (a) SC1 phase at  $J_2 = 0.01$ . (b), (c) Isotropic  $d + id$ -wave TSC phase at  $J_2 = 0.05$  with near-isotropic structure. (d), (e) Nematic TSC phase at  $J_2 = 0.1$ . (f) SC0 state at  $J_2 = 0.2$ . The first Brillouin zone is indicated by the solid line with the  $\mathbf{M}$  and  $\mathbf{K}$  points marked, and the black dots represent the allowed discrete momenta for the finite system with  $12 \times 6$  sites. The results are obtained with  $M = 10000$ . The doping level is  $\delta = 1/12$ .

$J_2 = 0.01, J_\chi = 0.05$  inside the SC1 phase, while the spin correlations exponentially decay at long distance for all three classes of SC phases (see Supplemental Sec. III. E [62] for details). With a larger  $J_2 = 0.05$  in the SC2 phase,  $S(\mathbf{k})$  becomes nearly featureless with some intensity around the Brillouin zone boundaries as shown in Figs. 7(b) and 7(c), which is consistent with an isotropic  $d + id$ -wave TSC state. As  $J_2$  further increases to 0.1, moderate peaks appear in  $S(\mathbf{k})$  at the  $\mathbf{M}$  points with nematicity as seen in Figs. 7(d) and 7(e), where the SC pairing order parameters also become anisotropic [Fig. 5(d)]. Further increasing  $J_2$  into the SC0 phase, the spin fluctuations appear as brighter peaks in  $S(\mathbf{k})$  at the  $\mathbf{M}$  points, with stronger stripe fluctuations as shown in Fig. 7(f). The emerging picture is that the spin nematicity tuned by hole dynamics (see more details in the Supplemental Sec. IV [62]) and spin interactions with the increase of  $J_2$  (and  $t_2$ ) are the determining forces in driving the quantum phase transitions between different SC phases.

## V. SUMMARY AND DISCUSSION

We have extensively studied the ground state of the lightly doped extended  $t$ - $J$ - $J_\chi$  model on the triangular lattice based on the state-of-the-art DMRG method and unraveled a global picture of emergent unconventional superconductivity in systems with chiral interactions that could be induced by an external magnetic field [32]. We identify three classes of superconducting phases (SC1, SC2, and SC0) characterized by different

topological Chern numbers and pairing symmetries. As next nearest neighbor hopping  $t_2$  and the related spin coupling  $J_2$  increase, the critical SC1 state with Chern number  $C = 1$  has a transition to the isotropic TSC phase, which is a gapped topological  $d + id$ -wave superconductor with  $C = 2$ . With further increase of  $t_2$  and  $J_2$ , the isotropic TSC state has a transition to a nematic TSC state in the smaller  $J_\chi$  regime, which is an analogy of the nematic fractional quantum Hall state with broken rotational symmetry [66–68]. A topological phase transition from the  $C = 2$  TSC states to the nematic  $d$ -wave SC0 state with  $C = 0$  occurs for larger  $t_2$  and  $J_2$ . The hole dynamics tuned by next-nearest-neighboring hoppings and spin couplings drives the topological quantum phase transitions between different SC phases, and a small chiral interaction  $J_\chi \approx 0.01$  stabilizes the SC states.

The TSC is a long-sought state, and it was conjectured that such a SC state may be realized by doping a CSL [48, 49] if it can win over other competing states varying from a chiral metal [11, 34] to a fractionalized Wigner crystal [57, 74]. Despite intensive efforts in searching for such a TSC state in strongly correlated systems during the past decades, there is only one established example by unbiased numerical studies of the  $t$ - $J$ - $J_\chi$  model [32]. The identified TSC state also showed some instability on a wider cylinder ( $L_y = 6$ ) [32] before adding next-nearest-neighboring hopping, indicating that it is near a phase boundary. In this work, we uncover a global phase diagram for the same model and unravel two distinct classes of TSC phases with Chern numbers  $C = 1, 2$ , and a nematic  $d$ -wave SC phase with  $C = 0$ . The new insight to the mechanism of the doping-induced TSC is that the TSC can emerge by doping a correlated Mott insulating state with  $120^\circ$  AFM besides doping a CSL state. Importantly, the hole dynamics changes the spin background and induces a topological quantum phase transition upon doping a magnetic ordered state, widening the opportunity for discovering TSC in triangular compounds. On the other hand, nematic SC with  $C = 0$  can emerge from either doping the CSL or magnetic ordered states [53], suggesting the rich interplay between unconventional SC and spin background.

A recent analytical study [46] has identified topological and nematic SC in the moiré superlattice of twisted bilayer TMD that realizes an effective triangular lattice model with repulsive interactions. While the study addresses the physics in the weak coupling picture with spin-valley fluctuations, it is interesting to see the  $C = 2$  topological  $d + id$ -wave SC and the nematic  $d$ -wave SC being discovered, which may indicate a possible universal picture for SC on triangular lattice with repulsive interactions. It would be exciting to examine the extended Hubbard model with short-range Coulomb interactions for such systems from weak to strong couplings [7], which can make further predictions for TMD systems. In light of the theoretical prediction of the SU(4) CSL [75] in time-reversal-invariant TMD bilayers, we anticipate TSC

to be a strong competing state and a rich phase diagram to be revealed. Besides the triangular lattice, it will also be interesting to search for possible TSC states in other systems including kagome compounds, where Mott insulators show similar rich physics with emergent CSL [52].

## ACKNOWLEDGMENTS

We thank Z. Q. Wang and Yahui Zhang for stimulating discussions. This work was supported by the U.S. Department of Energy, Office of Basic Energy Sciences under Grant No. DE-FG02-06ER46305.

- 
- [1] P. W. Anderson, The resonating valence bond state in  $\text{La}_2\text{CuO}_4$  and superconductivity, *Science* **235**, 1196 (1987).
- [2] P. A. Lee, N. Nagaosa, and X.-G. Wen, Doping a mott insulator: Physics of high-temperature superconductivity, *Reviews of modern physics* **78**, 17 (2006).
- [3] B. Keimer, S. A. Kivelson, M. R. Norman, S. Uchida, and J. Zaanen, From quantum matter to high-temperature superconductivity in copper oxides, *Nature* **518**, 179 (2015).
- [4] C. Proust and L. Taillefer, The remarkable underlying ground states of cuprate superconductors, *Annual Review of Condensed Matter Physics* **10**, 409 (2019).
- [5] M. Ogata and H. Fukuyama, The  $t$ - $j$  model for the oxide high- $T_c$  superconductors, *Reports on Progress in Physics* **71**, 036501 (2008).
- [6] E. Fradkin, S. A. Kivelson, and J. M. Tranquada, Colloquium: Theory of intertwined orders in high temperature superconductors, *Reviews of Modern Physics* **87**, 457 (2015).
- [7] D. P. Arovas, E. Berg, S. A. Kivelson, and S. Raghu, The hubbard model, *Annual Review of Condensed Matter Physics* **13**, 239 (2022).
- [8] L. Balents, Spin liquids in frustrated magnets, *Nature* **464**, 199 (2010).
- [9] T. Senthil and P. A. Lee, Cuprates as doped  $u(1)$  spin liquids, *Phys. Rev. B* **71**, 174515 (2005).
- [10] Z. Weng, D. Sheng, and C. Ting, Mean-field description of the phase string effect in the  $t$ - $j$  model, *Physical Review B* **59**, 8943 (1999).
- [11] X.-Y. Song, A. Vishwanath, and Y.-H. Zhang, Doping the chiral spin liquid: Topological superconductor or chiral metal, *Physical Review B* **103**, 165138 (2021).
- [12] S. R. White and D. J. Scalapino, Pairing on striped  $t$ - $t'$ - $j$  lattices, *Physical Review B* **79**, 220504(R) (2009).
- [13] P. Corboz, T. M. Rice, and M. Troyer, Competing states in the  $t$ - $j$  model: Uniform  $d$ -wave state versus stripe state, *Physical review letters* **113**, 046402 (2014).
- [14] J. P. F. LeBlanc, A. E. Antipov, F. Becca, I. W. Bulik, G. K.-L. Chan, C.-M. Chung, Y. Deng, M. Ferrero, T. M. Henderson, C. A. Jiménez-Hoyos, E. Kozik, X.-W. Liu, A. J. Millis, N. V. Prokof'ev, M. Qin, G. E. Scuseria, H. Shi, B. V. Svistunov, L. F. Tocchio, I. S. Tupitsyn, S. R. White, S. Zhang, B.-X. Zheng, Z. Zhu, and E. Gull (Simons Collaboration on the Many-Electron Problem), Solutions of the two-dimensional hubbard model: Benchmarks and results from a wide range of numerical algorithms, *Phys. Rev. X* **5**, 041041 (2015).
- [15] H.-C. Jiang and T. P. Devereaux, Superconductivity in the doped hubbard model and its interplay with next-nearest hopping  $t'$ , *Science* **365**, 1424 (2019).
- [16] M. Qin, C.-M. Chung, H. Shi, E. Vitali, C. Hubig, U. Schollwöck, S. R. White, and S. Zhang (Simons Collaboration on the Many-Electron Problem), Absence of superconductivity in the pure two-dimensional hubbard model, *Phys. Rev. X* **10**, 031016 (2020).
- [17] B.-X. Zheng, C.-M. Chung, P. Corboz, G. Ehlers, M.-P. Qin, R. M. Noack, H. Shi, S. R. White, S. Zhang, and G. K.-L. Chan, Stripe order in the underdoped region of the two-dimensional hubbard model, *Science* **358**, 1155 (2017).
- [18] H.-C. Jiang, Z.-Y. Weng, and S. A. Kivelson, Superconductivity in the doped  $t$ - $j$  model: Results for four-leg cylinders, *Physical Review B* **98**, 140505(R) (2018).
- [19] J. F. Dodaro, H.-C. Jiang, and S. A. Kivelson, Intertwined order in a frustrated four-leg  $t$ - $j$  cylinder, *Physical Review B* **95**, 155116 (2017).
- [20] Y.-F. Jiang, J. Zaanen, T. P. Devereaux, and H.-C. Jiang, Ground state phase diagram of the doped hubbard model on the four-leg cylinder, *Physical Review Research* **2**, 033073 (2020).
- [21] H.-C. Jiang and S. A. Kivelson, High temperature superconductivity in a lightly doped quantum spin liquid, *Phys. Rev. Lett.* **127**, 097002 (2021).
- [22] S. Gong, W. Zhu, and D. N. Sheng, Robust  $d$ -wave superconductivity in the square-lattice  $t$ - $j$  model, *Phys. Rev. Lett.* **127**, 097003 (2021).
- [23] S. Jiang, D. J. Scalapino, and S. R. White, Ground-state phase diagram of the  $tt'$ - $j$  model, *Proceedings of the National Academy of Sciences* **118**, e2109978118 (2021).
- [24] S. R. White, Density matrix formulation for quantum renormalization groups, *Physical review letters* **69**, 2863 (1992).
- [25] G. Baskaran, Electronic model for  $\text{CoO}_2$  layer based systems: Chiral resonating valence bond metal and superconductivity, *Physical review letters* **91**, 097003 (2003).
- [26] B. Kumar and B. S. Shastry, Superconductivity in  $\text{CoO}_2$  layers and the resonating valence bond mean-field theory of the triangular lattice  $t$ - $j$  model, *Physical Review B* **68**, 104508 (2003).
- [27] Q.-H. Wang, D.-H. Lee, and P. A. Lee, Doped  $t$ - $j$  model on a triangular lattice: Possible application to  $\text{Na}_x\text{CoO}_2$  and  $\text{Na}_1-x\text{TiO}_2$ , *Physical Review B* **69**, 092504 (2004).
- [28] O. I. Motrunich and P. A. Lee, Possible effects of charge frustration in  $\text{Na}_x\text{CoO}_2$ : Bandwidth suppression, charge orders, and resurrected resonating valence bond superconductivity, *Phys. Rev. B* **69**, 214516 (2004).
- [29] S. Raghu, S. A. Kivelson, and D. J. Scalapino, Superconductivity in the repulsive hubbard model: An asymptotically exact weak-coupling solution, *Physical Review B* **81**, 224505 (2010).
- [30] K. S. Chen, Z. Y. Meng, U. Yu, S. Yang, M. Jarrell, and J. Moreno, Unconventional superconductivity on the triangular lattice hubbard model, *Physical Review B* **88**, 041103(R) (2013).
- [31] J. Venderley and E.-A. Kim, Density matrix renormal-

- ization group study of superconductivity in the triangular lattice hubbard model, *Physical Review B* **100**, 060506(R) (2019).
- [32] Y.-F. Jiang and H.-C. Jiang, Topological superconductivity in the doped chiral spin liquid on the triangular lattice, *Physical Review Letters* **125**, 157002 (2020).
- [33] H.-C. Jiang, Superconductivity in the doped quantum spin liquid on the triangular lattice, *npj Quantum Materials* **6**, 71 (2021).
- [34] Z. Zhu, D. N. Sheng, and A. Vishwanath, Doped mott insulators in the triangular-lattice hubbard model, *Physical Review B* **105**, 205110 (2022).
- [35] Y. Gannot, Y.-F. Jiang, and S. A. Kivelson, Hubbard ladders at small  $u$  revisited, *Phys. Rev. B* **102**, 115136 (2020).
- [36] A. Szasz, J. Motruk, M. P. Zaletel, and J. E. Moore, Chiral spin liquid phase of the triangular lattice hubbard model: a density matrix renormalization group study, *Physical Review X* **10**, 021042 (2020).
- [37] B.-B. Chen, Z. Chen, S.-S. Gong, D. Sheng, W. Li, and A. Weichselbaum, Quantum spin liquid with emergent chiral order in the triangular-lattice hubbard model, *arXiv preprint arXiv:2102.05560* (2021).
- [38] C. Peng, Y.-F. Jiang, Y. Wang, and H.-C. Jiang, Gapless spin liquid and pair density wave of the hubbard model on three-leg triangular cylinders, *New Journal of Physics* **23**, 123004 (2021).
- [39] A. Wietek, R. Rossi, F. Šimkovic, M. Klett, P. Hansmann, M. Ferrero, E. M. Stoudenmire, T. Schäfer, and A. Georges, Mott insulating states with competing orders in the triangular lattice hubbard model, *Phys. Rev. X* **11**, 041013 (2021).
- [40] A. M. Aghaei, B. Bauer, K. Shtengel, and R. V. Mishmash, Efficient matrix-product-state preparation of highly entangled trial states: Weak mott insulators on the triangular lattice revisited, *arXiv preprint arXiv:2009.12435* (2020).
- [41] K. Takada, H. Sakurai, E. Takayama-Muromachi, F. Izumi, R. A. Dilanian, and T. Sasaki, Superconductivity in two-dimensional  $coo_2$  layers, *Nature* **422**, 53 (2003).
- [42] S. Zhou and Z. Wang, Nodal  $d+id$  pairing and topological phases on the triangular lattice of  $na_xcoo_2 \cdot y_h_2o$ : evidence for an unconventional superconducting state, *Physical review letters* **100**, 217002 (2008).
- [43] F. Wu, T. Lovorn, E. Tutuc, and A. H. MacDonald, Hubbard model physics in transition metal dichalcogenide moiré bands, *Physical review letters* **121**, 026402 (2018).
- [44] Y. Tang, L. Li, T. Li, Y. Xu, S. Liu, K. Barmak, K. Watanabe, T. Taniguchi, A. H. MacDonald, J. Shan, and K. F. Mak, Simulation of hubbard model physics in  $wse_2/ws_2$  moiré superlattices, *Nature* **579**, 353 (2020).
- [45] L. An, X. Cai, D. Pei, M. Huang, Z. Wu, Z. Zhou, J. Lin, Z. Ying, Z. Ye, X. Feng, *et al.*, Interaction effects and superconductivity signatures in twisted double-bilayer  $wse_2$ , *Nanoscale horizons* **5**, 1309 (2020).
- [46] C. Schrade and L. Fu, Nematic, chiral and topological superconductivity in transition metal dichalcogenides, *arXiv preprint arXiv:2110.10172* (2021).
- [47] M. M. Scherer, D. M. Kennes, and L. Classen,  $N=4$  chiral superconductivity in moiré transition metal dichalcogenides, *arXiv preprint arXiv:2108.11406* (2021).
- [48] V. Kalmeyer and R. B. Laughlin, Equivalence of the resonating-valence-bond and fractional quantum hall states, *Physical review letters* **59**, 2095 (1987).
- [49] X.-G. Wen, F. Wilczek, and A. Zee, Chiral spin states and superconductivity, *Physical Review B* **39**, 11413 (1989).
- [50] B. Bauer, L. Cincio, B. Keller, M. Dolfi, G. Vidal, S. Trebst, and A. Ludwig, Chiral spin liquid and emergent anyons in a kagome lattice mott insulator, *Nature Communications* **5**, 10.1038/ncomms6137 (2014).
- [51] Y.-C. He, D. N. Sheng, and Y. Chen, Chiral spin liquid in a frustrated anisotropic kagome heisenberg model, *Phys. Rev. Lett.* **112**, 137202 (2014).
- [52] S.-S. Gong, W. Zhu, and D. N. Sheng, Emergent chiral spin liquid: Fractional quantum hall effect in a kagome heisenberg model, *Scientific Reports* **4**, 10.1038/srep06317 (2014).
- [53] S.-S. Gong, W. Zhu, J.-X. Zhu, D. N. Sheng, and K. Yang, Global phase diagram and quantum spin liquids in a spin-1/2 triangular antiferromagnet, *Physical Review B* **96**, 075116 (2017).
- [54] A. Wietek and A. M. Läuchli, Chiral spin liquid and quantum criticality in extended  $s=1/2$  heisenberg models on the triangular lattice, *Physical Review B* **95**, 035141 (2017).
- [55] R. B. Laughlin, Superconducting ground state of non-interacting particles obeying fractional statistics, *Phys. Rev. Lett.* **60**, 2677 (1988).
- [56] D.-H. Lee and M. P. A. Fisher, Anyon superconductivity and the fractional quantum hall effect, *Phys. Rev. Lett.* **63**, 903 (1989).
- [57] H.-C. Jiang, T. Devereaux, and S. A. Kivelson, Holon wigner crystal in a lightly doped kagome quantum spin liquid, *Phys. Rev. Lett.* **119**, 067002 (2017).
- [58] N. Read and D. Green, Paired states of fermions in two dimensions with breaking of parity and time-reversal symmetries and the fractional quantum hall effect, *Physical Review B* **61**, 10267 (2000).
- [59] T. Senthil, J. B. Marston, and M. P. A. Fisher, Spin quantum hall effect in unconventional superconductors, *Physical Review B* **60**, 4245 (1999).
- [60] A. Luther and V. Emery, Backward scattering in the one-dimensional electron gas, *Physical Review Letters* **33**, 589 (1974).
- [61] I. P. McCulloch, From density-matrix renormalization group to matrix product states, *Journal of Statistical Mechanics: Theory and Experiment* **2007**, P10014 (2007).
- [62] See Supplemental Material at <http://link.aps.org/supplemental/10.1103/PhysRevX.12.031009> for detailed numerical results.
- [63] A. G. Grushin, J. Motruk, M. P. Zaletel, and F. Pollmann, Characterization and stability of a fermionic  $\nu=1/3$  fractional chern insulator, *Physical Review B* **91**, 035136 (2015).
- [64] For  $J_2 < 0.01$  or  $J_\chi < 0.01$ , it becomes increasingly difficult to obtain converged ground state or identify phase boundaries.
- [65] F. D. M. Haldane, Geometrical description of the fractional quantum hall effect, *Physical review letters* **107**, 116801 (2011).
- [66] Y. You, G. Y. Cho, and E. Fradkin, Theory of nematic fractional quantum hall states, *Physical Review X* **4**, 041050 (2014).
- [67] B. Yang, C. H. Lee, C. Zhang, and Z.-X. Hu, Anisotropic pseudopotential characterization of quantum hall systems under a tilted magnetic field, *Physical Review B* **96**, 195140 (2017).

- [68] N. Regnault, J. Maciejko, S. A. Kivelson, and S. L. Sondhi, Evidence of a fractional quantum hall nematic phase in a microscopic model, *Physical Review B* **96**, 035150 (2017).
- [69] D. N. Sheng, Z. Y. Weng, L. Sheng, and F. D. M. Haldane, Quantum spin-hall effect and topologically invariant chern numbers, *Phys. Rev. Lett.* **97**, 036808 (2006).
- [70] W.-J. Hu, W. Zhu, Y. Zhang, S. Gong, F. Becca, and D. N. Sheng, Variational monte carlo study of a chiral spin liquid in the extended heisenberg model on the kagome lattice, *Physical Review B* **91**, 041124(R) (2015).
- [71] U. Schollwöck, The density-matrix renormalization group in the age of matrix product states, *Annals of physics* **326**, 96 (2011).
- [72] G.-Q. Zhong, S.-S. Gong, Q.-R. Zheng, and G. Su, Quantum phase transitions in a spin-1/2 alternating heisenberg antiferromagnetic chain under a staggered transverse magnetic field, *Physics Letters A* **373**, 1687 (2009).
- [73] J. Zhang, Fidelity and entanglement entropy for infinite-order phase transitions, *Physical Review B* **104**, 205112 (2021).
- [74] C. Peng, Y. Jiang, D. Sheng, and H. Jiang, Doping quantum spin liquids on the kagome lattice, *Advanced Quantum Technologies* **4**, 2000126 (2021).
- [75] Y.-H. Zhang, D. N. Sheng, and A. Vishwanath, Su (4) chiral spin liquid, exciton supersolid, and electric detection in moiré bilayers, *Physical review letters* **127**, 247701 (2021).

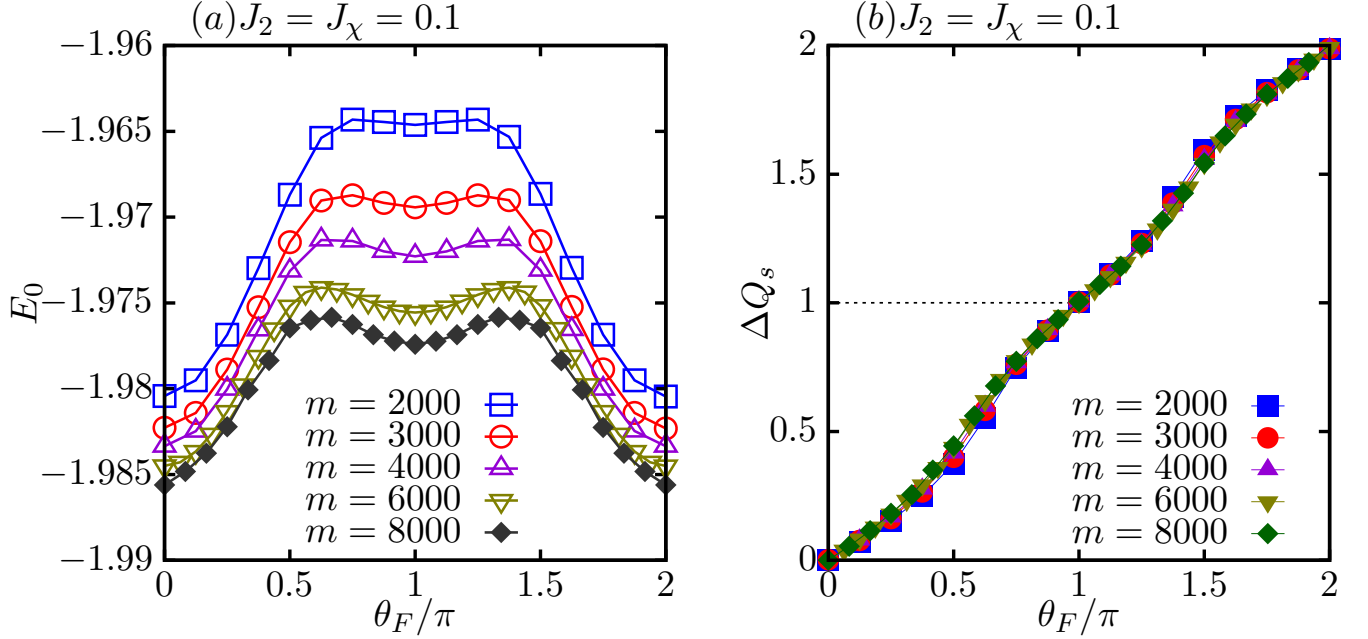


FIG. S1. (a) The energy per site  $E_0$ . (b) The spin pumping  $\Delta Q_s$  versus flux  $\theta_F$  for various bond dimension  $m$ . Results are obtained at  $J_2 = J_\chi = 0.1$  and  $\delta = 1/12$  on  $L_y = 6$  infinite cylinder.

## Supplementary for “Topological chiral and nematic superconductivity by doping Mott insulators on triangular lattice”

### i. ROBUST SPIN PUMPING WITH FLUX INSERTION

The flux insertion method has been extensively applied to different fractional quantum Hall and chiral spin liquid systems to study the topological nature. Here we demonstrate the robustness of the method when we apply it to the topological superconducting states of the doped triangular  $t$ - $J$ - $J_\chi$  model as defined in the main text. Because the inserted flux breaks  $SU(2)$  symmetry, we use infinite DMRG with  $U(1) \times U(1)$  symmetries for both charge and spin degrees of freedom with a large unit cell commensurate with the doping level. We check the spin pumping versus inserting flux for various bond dimensions  $m$  to confirm the robustness of results. As shown in Fig. S1(a) at  $J_2 = J_\chi = 0.1$  and  $\delta = 1/12$  on  $L_y = 6$  cylinder, the ground state energy per site  $E_0$  varies smoothly with flux  $\theta_F$ , and  $E_0(\theta_F)$  curves have similar shapes for different  $m$ , indicating that the flux insertion simulations are less sensitive to bond dimension  $m$ . Indeed, we find that the pumped spin  $\Delta Q_s$  evolves with  $\theta_F$  smoothly with all curves almost fall on top of each other, which is insensitive to the bond dimension  $m$ . It gives rise to the same quantized Chern number  $C = 2$  after completing the insertion of one flux quantum for different  $m$  as shown in Fig. S1(b). We use a unit cell of  $4 \times L_y$  sites or  $8 \times L_y$  sites for the doping level  $\delta = 1/12$  on  $L_y = 6$ , which always gives the same quantized results.

### ii. ENERGY CONVERGENCE OF THE GROUND STATE WITH INCREASING BOND DIMENSION

We use the finite size DMRG with the  $U(1) \times SU(2)$  symmetries to study the ground state properties of the doped triangular  $t$ - $J$ - $J_\chi$  model. Here we show an example of the ground state energy convergence with the increase of the bond dimensions  $M = 3000 \sim 12000$  (which are equivalent to  $m = 9000 \sim 36000$   $U(1)$  states) for a system with  $N = 36 \times 6$ . As shown in Fig. S2, we demonstrate the obtained energy per site  $E_0$  (measured in the middle  $12 \times 6$  sites) versus the DMRG truncation error. With  $M = 12000$ , the truncation error is reduced to about  $4 \times 10^{-6}$ . The extrapolated energy  $-1.98785$  is also close to the lowest energy that we obtain with  $M = 12000$ , indicating the good convergence of our calculations.

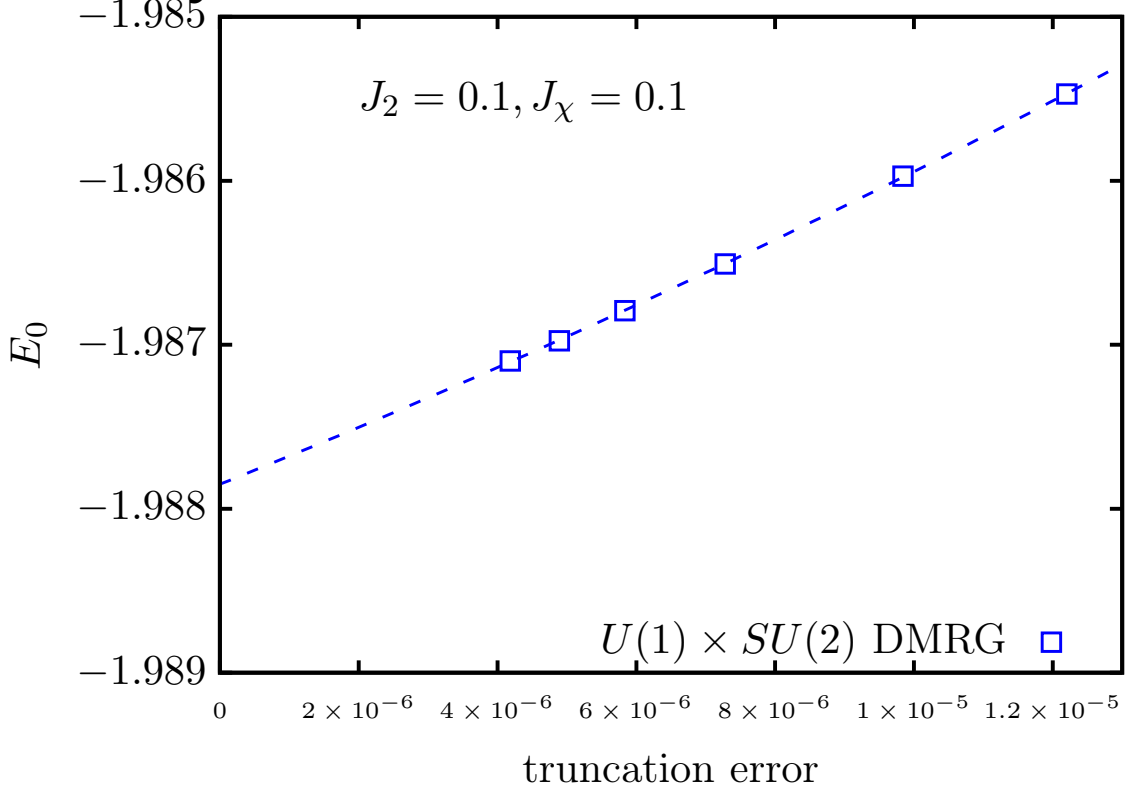


FIG. S2. The ground state energy per site  $E_0$  calculated based on  $U(1) \times SU(2)$  DMRG for various bond dimension  $M$ , obtained at  $J_2 = J_\chi = 0.1$  and  $\delta = 1/12$  for  $N = 36 \times 6$  system.

### iii. MORE EXAMPLES OF CORRELATION FUNCTIONS IN DIFFERENT PHASES

#### A. Results of correlation functions in various systems sizes for SC2 phase with $J_2 = 0.1$ and $J_\chi = 0.05$

Results on different system sizes are presented here to compare with the results in the main text at  $J_2 = 0.1, J_\chi = 0.05$  on  $N = 36 \times 6$  system and  $\delta = 1/12$ . As shown in Fig. S3, we study similar correlation functions on a shorter system  $N = 24 \times 6$ . The superconductivity (SC) pairing correlations in Fig. S3(a) show a quasi-long-range power-law decay after the scaling to  $M \rightarrow \infty$ , with a Luttinger exponent  $K_{SC} \approx 0.76$  the same as the result on  $L_x = 36$  in the main text. The ratio between the magnitudes of SC pairing correlations for different bonds also have almost the same average values as those on  $L_x = 36$ , indicating a small finite size effect on the length of  $L_x$ . Furthermore, the density-density correlation  $D(\mathbf{r}) = \langle \hat{n}_{\mathbf{r}_0} \hat{n}_{\mathbf{r}_0 + \mathbf{r}} \rangle - \langle \hat{n}_{\mathbf{r}_0} \rangle \langle \hat{n}_{\mathbf{r}_0 + \mathbf{r}} \rangle$ , single particle correlation  $G(\mathbf{r}) = \langle \sum_{\sigma} \hat{c}_{\mathbf{r}_0, \sigma}^\dagger \hat{c}_{\mathbf{r}_0 + \mathbf{r}, \sigma} \rangle$ , and the spin correlation  $S(\mathbf{r}) = \langle \hat{\mathbf{S}}_{\mathbf{r}_0} \cdot \hat{\mathbf{S}}_{\mathbf{r}_0 + \mathbf{r}} \rangle$  also show near the same decaying behaviors as the results on  $L_x = 36$ . Specifically, we can fit the  $|G(r)|$  with both exponential decay and power-law decay functions, as shown in Figs. S3(b) and (d). Under the exponential decay fitting, the correlation length  $\xi_G \approx 6.57$ , which is already larger than the system width  $L_y = 6$ , which could also be fit with power-law decay. In comparison, the  $|S(r)|$  given in Fig. S3(d) has a correlation length of  $\xi_S = 1.43$  which is much smaller than the system width  $L_y$  indicating fast exponential decay for spin correlations.

The finite bond dimension scaling of different physical quantities are used to obtain accurate results of the ground state. Here we show the details in the scaling of correlations versus  $1/M$  for two typical examples  $|P_{bb}(r)|$  and  $D(r)$  using the polynomial fitting up to the second order of  $1/M$ . As shown in Fig. S4 on different  $L_x = 24$  and  $36$  with  $L_y = 6$ , the  $|P_{bb}(r)|$  and  $D(r)$  vary smoothly with increasing  $M$  and can be reliably extrapolated to the infinite  $M$  limit.

Besides studies on  $L_y = 6$ , we also find consistent results on  $L_y = 4$  systems. As shown in Fig. S5, the same decay patterns are found for all correlation functions comparing  $L_y = 4$  with  $L_y = 6$  results (shown in the main

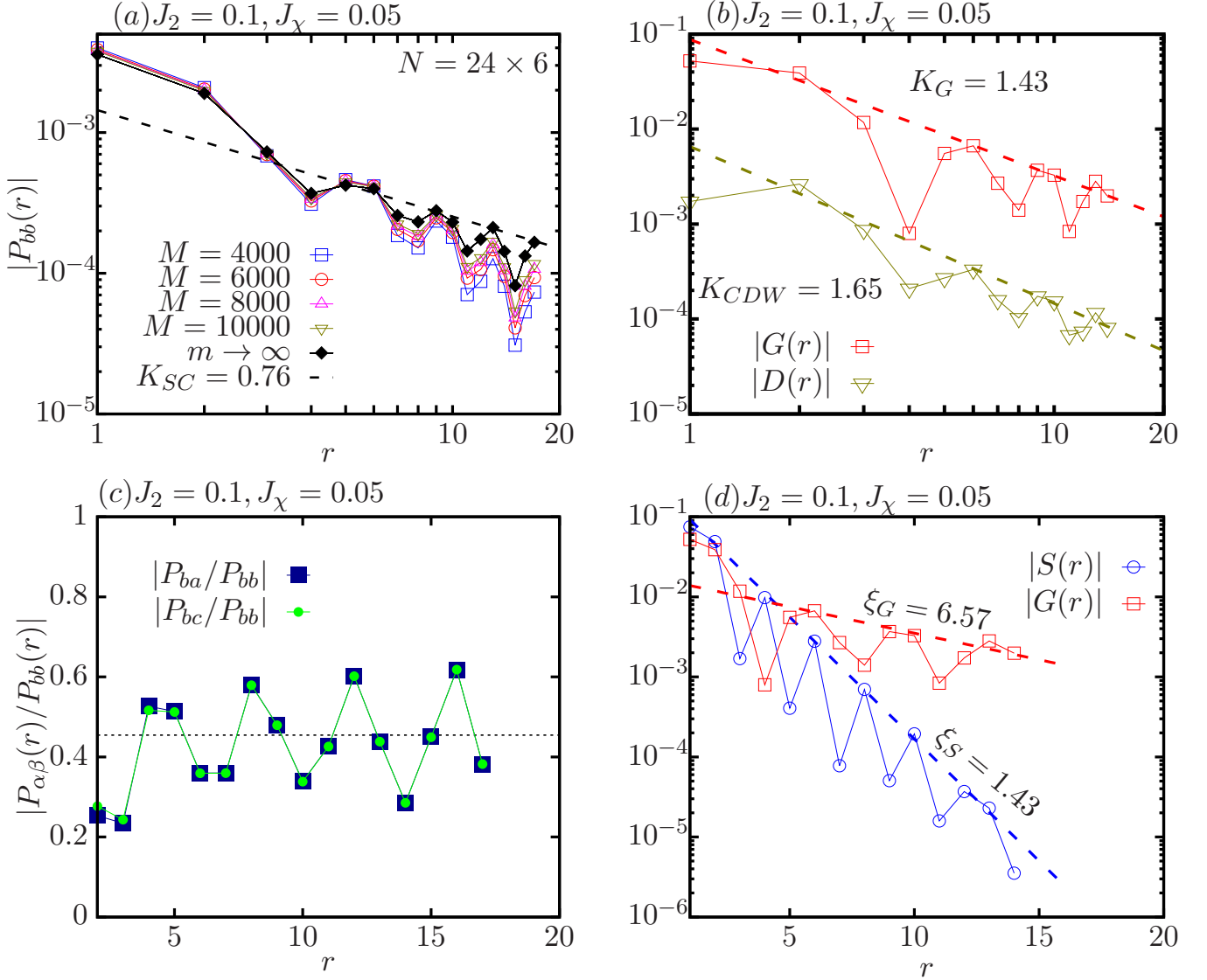


FIG. S3. Various correlation functions on  $N = 24 \times 6$  system, obtained at  $J_2 = 0.1, J_\chi = 0.05$ .  $\mathbf{r}$  is chosen along x-direction  $\mathbf{r} = (r, 0)$ . (a) The scaling of SC pairing correlation with bond dimension  $M$ . The Luttinger exponent is obtained by the straight-line fitting in the log-log plot for the extrapolated infinite  $M$  data. (b) The density-density correlation  $|D(r)|$  and single particle correlation  $|G(r)|$ , which are also fit by the power-law relations. (c) The ratio between the magnitudes of SC pairing correlations for different bonds. The dash line indicates the spatial average over distances. (d) The exponential fitting of the spin correlation  $|S(r)|$  and  $|G(r)|$ .

text), indicating a robust quasi-long-range SC order dominating other correlations. In particular, the SC Luttinger exponent  $K_{SC} = 0.89$  on  $L_y = 4$ , which is larger than  $K_{SC} = 0.76$  on  $L_y = 6$  ( $L_x = 36$ ) at the same parameter point  $J_2 = 0.1, J_\chi = 0.05$ , which suggests a stronger SC on wider cylinders.

### B. Results of correlation functions for additional points in SC2 phase

We provide more evidence of the quasi-long-range SC order on  $N = 36 \times 6$  system at  $\delta = 1/12$ . Figure S6 shows various correlation functions at  $J_2 = J_\chi = 0.05$  in the SC2 phase for an isotropic gapped topological  $d + id$ -wave SC state on  $L_y = 6$ . Similar to the results at  $J_2 = 0.1, J_\chi = 0.05$ , the SC pairing correlation has power-law decaying behavior in the infinite  $M$  limit, with the Luttinger exponent  $K_{SC} \approx 1.04$ . The  $|D(r)|$  could be approximately fit by

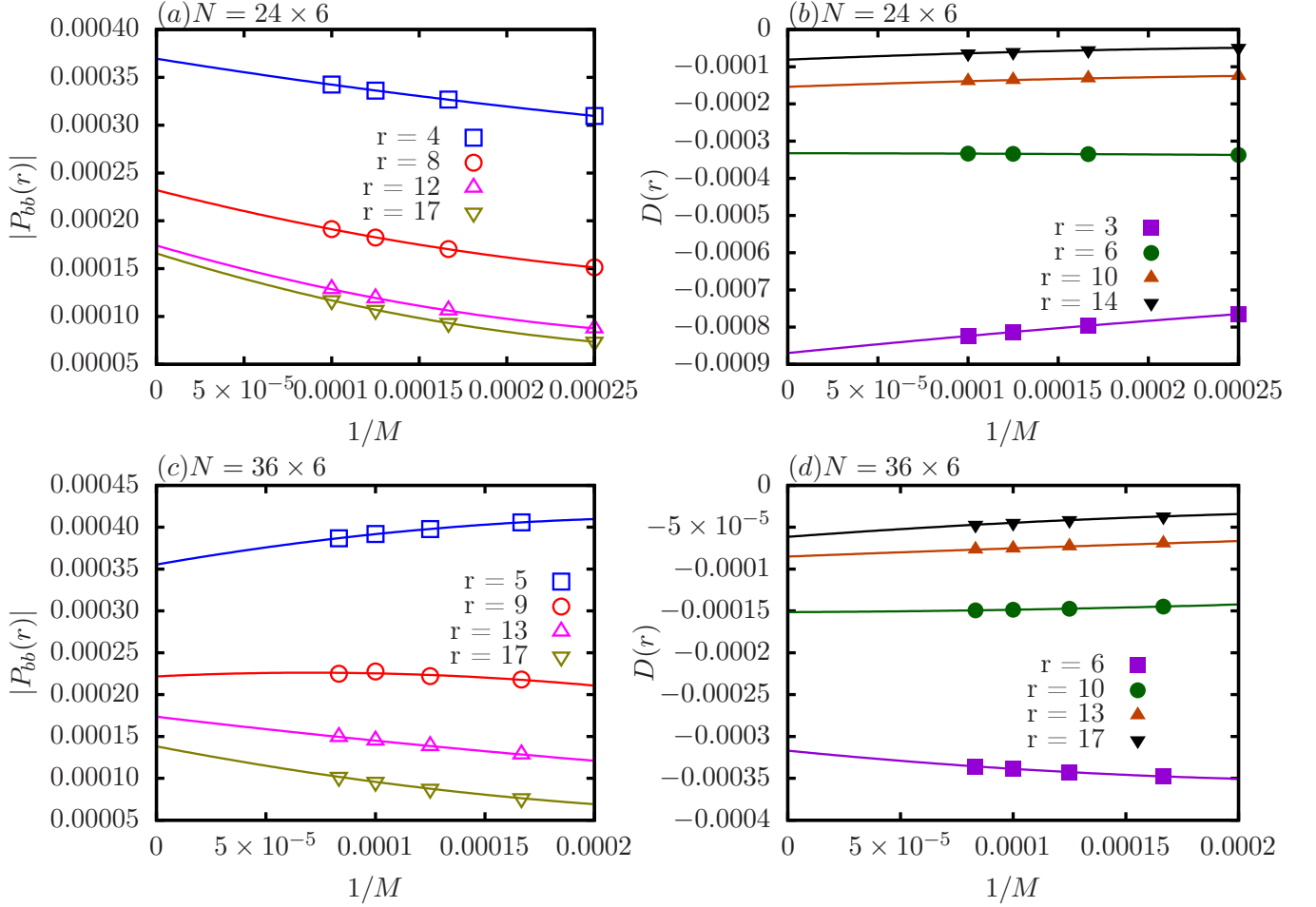


FIG. S4. The extrapolations of correlation functions at  $J_2 = 0.1, J_x = 0.05$  versus  $1/M$  for (a)  $|P_{bb}|$  and (b)  $D(r)$  on  $N = 24 \times 6$  system. (c) and (d) are similar extrapolations on  $N = 36 \times 6$  system.

power-law decay with  $K_{CDW} \approx 1.77 > K_{SC}$  and  $|D(r)|$  decays faster than power-law at long distances, confirming that the SC pairing correlation is the dominant correlation for this gapped isotropic topological SC state. The single particle correlation  $|G(r)|$  can be fit only by an exponential decay with a short correlation length  $\xi_G \approx 2.41$ . Similarly, the spin correlation  $|S(r)|$  has an exponential decay with a short correlation length  $\xi_S \approx 2.06$ .

As a comparison, we also show an anisotropic topological SC state at  $J_2 = J_x = 0.1$  in the SC2 phase in Fig. S7. Similar to the results at  $J_2 = 0.1, J_x = 0.05$ , the SC pairing correlation has power-law decaying behavior in the infinite  $M$  limit, with the Luttinger exponent  $K_{SC} \approx 0.79$ . The  $|D(r)|$  has power-law decay relation with  $K_{CDW} > K_{SC}$ . The single particle correlation  $|G(r)|$  can be fit either by a power-law or an exponential decay with a relatively long correlation length  $\xi_G \approx 7.21$ . The spin correlation  $|S(r)|$  has an exponential decay with a short correlation length  $\xi_S \approx 1.72$ .

### C. Results of correlation functions in SC0 phase

The correlation functions at larger  $J_2 = 0.2$  in the SC0 phase is given in Figs. S8(a) and (b). Both SC pairing correlations and density-density correlations follow the power-law behavior, with  $K_{SC} \approx 1.10$  much smaller than  $K_{CDW} \approx 2.02$ . The ratio between the magnitudes of SC pairing correlations for different bonds exhibit large spatial oscillations. As shown in Fig. S8(c), the maximum deviation from the average value of the ratio is around 0.52 at  $J_2 = 0.2, J_x = 0.2$ . In addition, the spin correlation  $|S(r)|$  has a relatively large correlation length of  $\xi_S = 5.90$  as shown in Fig. S8(d), which is slightly smaller than  $L_y = 6$ . These behaviors imply the reduced robustness of the SC state at this parameter point ( $J_2 = 0.2, J_x = 0.2$ ), which may be near the phase boundary to a non-superconducting

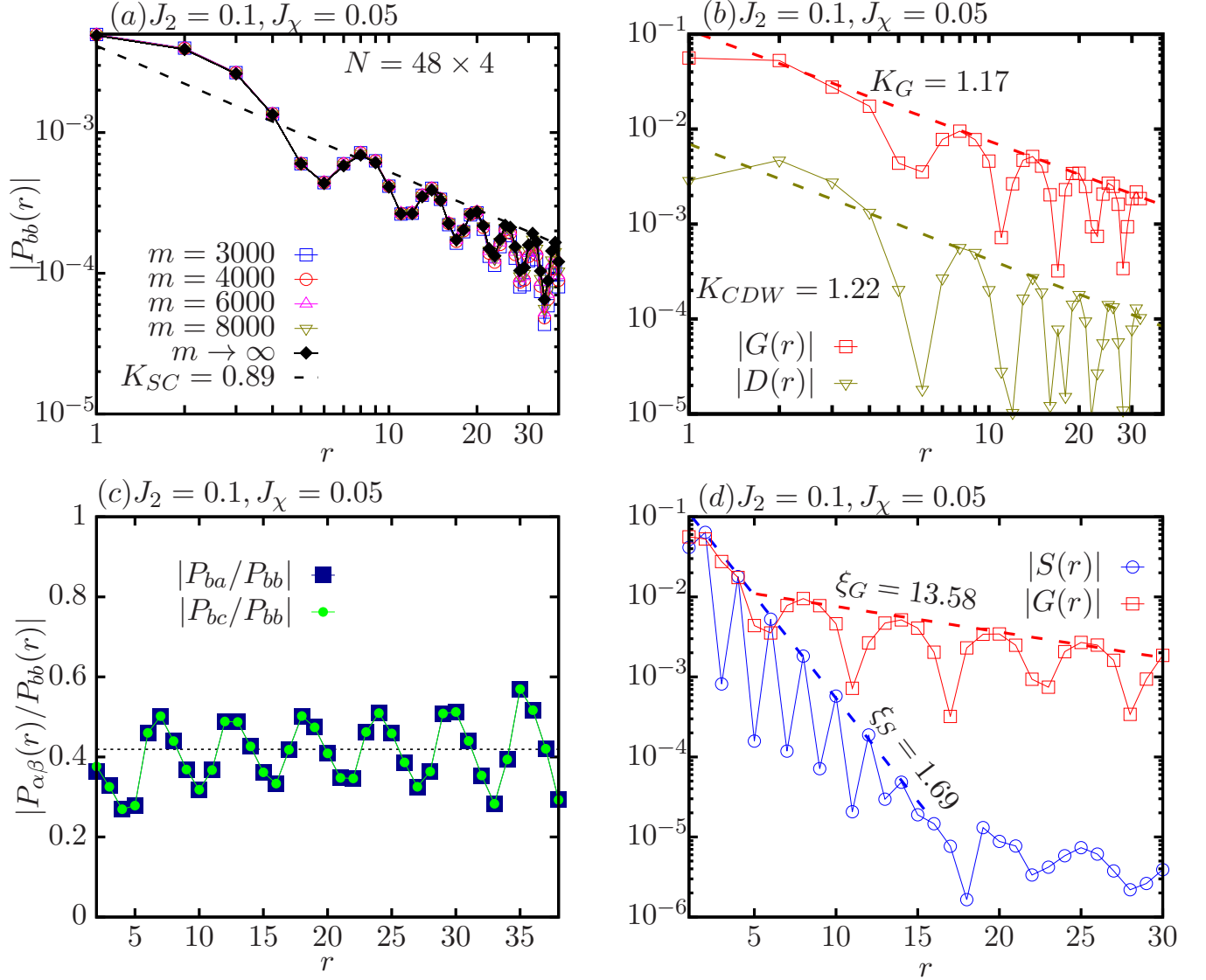


FIG. S5. Various correlations on  $N = 48 \times 4$  system, obtained at  $J_2 = 0.1, J_\chi = 0.05$ . (a) The scaling of SC pairing correlation with bond dimension  $M$ . The Luttinger exponent is obtained by the straight-line fitting in the log-log plot for the extrapolated infinite  $M$  data. (b) The density-density correlation  $|D(r)|$  and single particle correlation  $|G(r)|$ , which are also fit by the power-law relations. (c) The ratio between the magnitudes of SC pairing correlations for different bonds. The dash line indicates the spatial average over distances. (d) The exponential fitting of the spin correlation  $|S(r)|$  and  $|G(r)|$ .

state.

The SC0 phase can be connected to the d-wave superconductivity by doping the  $J_1$ - $J_2$  model at  $J_\chi = 0$  as studied in previous work [33], which are also shown in Figs. S9 and S10 for  $J_2 = 0.16$  and  $0.20$ , respectively. When  $J_2$  reaches  $0.2$ , there is a visible change in the ratio of pairing orders on different bonds, which signals some changes in the pairing symmetry with increasing  $J_2$ .

#### D. Results of correlation functions in SC1 phase

Various correlation functions at  $J_2 = 0.01, J_\chi = 0.05$  for a system with  $N = 20 \times 6$  are shown in Fig. S11. The SC pairing correlations  $|P_{bb}(r)|$  are strongly enhanced with the increase of the bond dimension as shown in Fig. S11(a), where the extrapolated data for infinite bond dimension shows a possible power-law behavior with the Luttinger

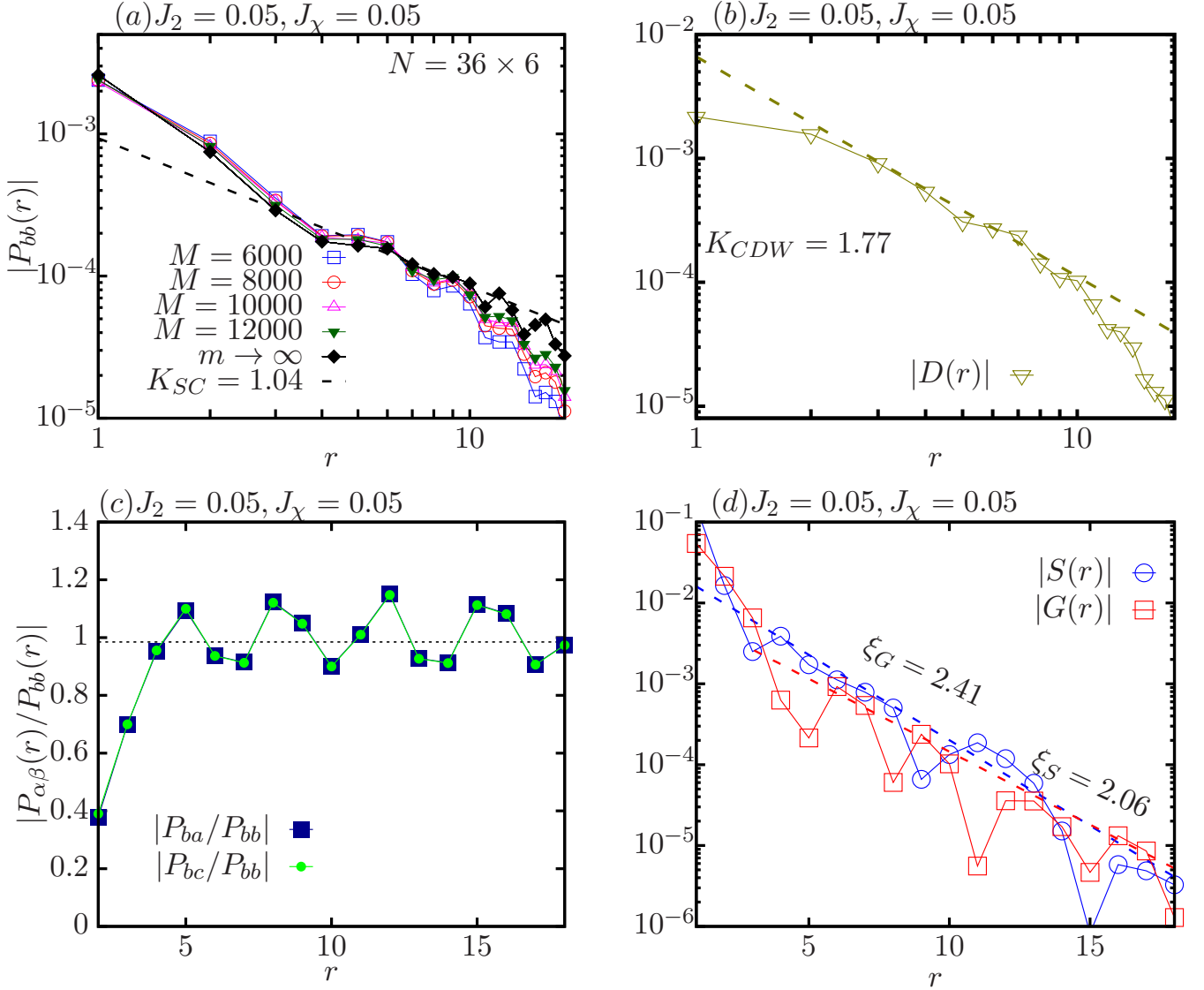


FIG. S6. Various correlations on  $N = 36 \times 6$  system, obtained at  $J_2 = 0.05, J_x = 0.05$ . (a) The scaling of SC pairing correlation with bond dimension  $M$ . The Luttinger exponent is obtained by the straight-line fitting in the log-log plot for the extrapolated infinite  $M$  data. (b) The density-density correlation  $|D(r)|$  is fit by the power-law relation at short distances. The  $|D(r)|$  decays faster for  $r > 10$ . (c) The ratio between the magnitudes of SC pairing correlations for different bonds. The dash line indicates the spatial average over distances. (d) The exponential fitting of the spin correlation  $|S(r)|$  and single particle correlation  $|G(r)|$ .

exponent  $K_{SC} \approx 1.19$ . The density-density correlations  $|D(r)|$  and single particle correlation  $|G(r)|$  can be fit by the power-law relations with larger exponents  $K_{CDW} \approx 1.75$  and  $K_G \approx 2.24$ , respectively, indicating dominant SC pairing correlations. The spin correlations are enhanced with a longer correlation length  $\xi_s \sim L_y$ . Noticing that this result is obtained on a system of a relatively short length with good convergence of the results. The full nature of the SC1 phase requires studying longer systems with larger bond dimensions due to the difficulty of the convergence for this possible critical phase.

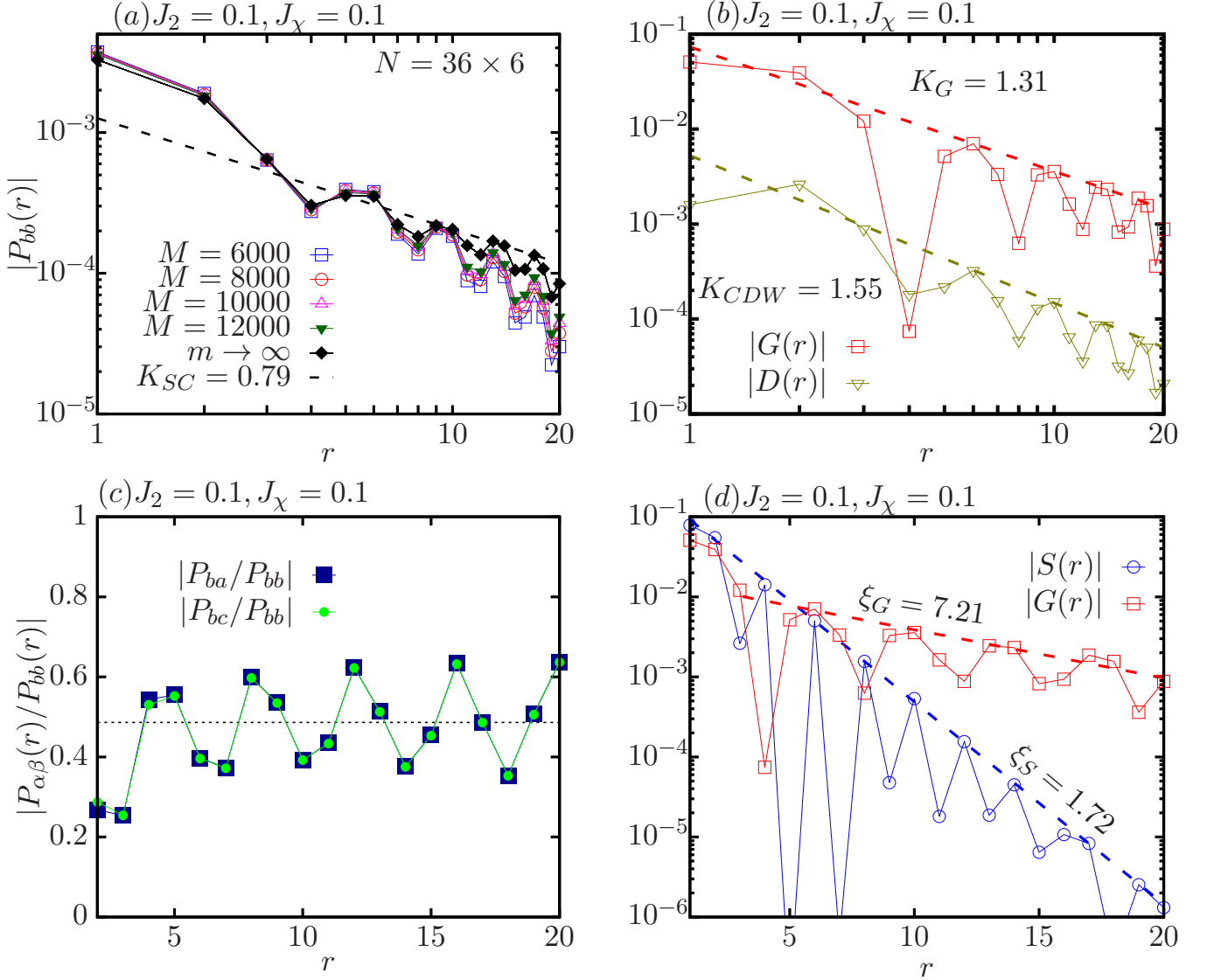


FIG. S7. Various correlations for  $N = 36 \times 6$  system, obtained at  $J_2 = 0.1, J_\chi = 0.1$ . (a) The scaling of SC pairing correlation with bond dimension  $M$ . The Luttinger exponent is obtained by the straight-line fitting in the log-log plot for the extrapolated infinite  $M$  data. (b) The density-density correlation  $|D(r)|$  and single particle correlation  $|G(r)|$ , which are also fit by the power-law relations. (c) The ratio between the magnitudes of SC pairing correlations for different bonds. The dash line indicates the spatial average over distances. (d) The exponential fitting of the spin correlation  $|S(r)|$  and  $|G(r)|$ .

### E. Comparison of spin correlations for all four phases

We describe the evolution of spin correlations with different parameters of  $J_2$  and  $J_\chi$ , as shown in Figs. S12(a) - (f). We find that the spin correlations always decay exponentially with a short correlation length in the SC2 regime indicating larger spin gaps crossing the whole topological superconducting phase with Chern number  $C = 2$ . The correlation length becomes larger entering the SC1 and SC0 phases, which is consistent with the enhanced peaks in spin structure factors presented in the main text.

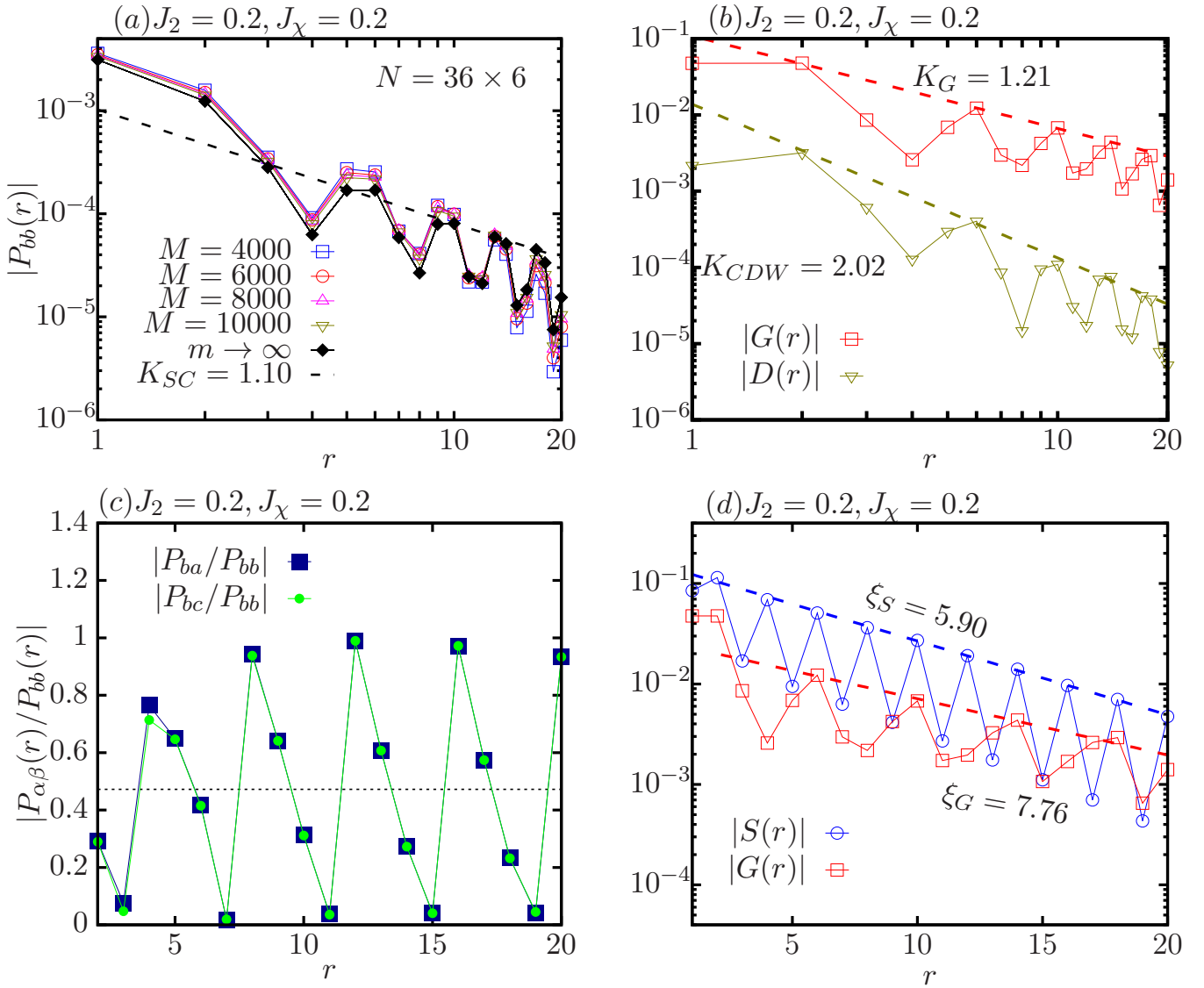


FIG. S8. Various correlations on  $N = 36 \times 6$  system, obtained at  $J_2 = 0.2, J_\chi = 0.2$ . (a) The scaling of SC pairing correlation with bond dimension  $M$ . The Luttinger exponent is obtained by the straight-line fitting in the log-log plot for the extrapolated infinite  $M$  data. (b) The density-density correlation  $|D(r)|$  and single particle correlation  $|G(r)|$ , which are also fit by the power-law relations. (c) The ratio between the magnitudes of SC pairing correlations for different bonds. The dash line indicates the spatial average over distances. (d) The exponential fitting of the spin correlation  $|S(r)|$  and  $|G(r)|$ .

### F. Exploring possible phases in the $J_\chi \rightarrow 0$ limit

There are different quantum phases emerging in the limit of  $J_\chi \rightarrow 0$ . With a small but finite  $J_2 = 0.01$  a possible pair density wave can be seen from the phases of SC pairing correlations. As shown in Fig. S13(a), the SC pairing correlation has a power-law decaying behavior for the a-a bond with the Luttinger exponent  $K_{SC} \approx 0.94$ . The  $|D(r)|$  could also be fit by power-law decay with  $K_{CDW} \approx 1.42 > K_{SC}$  (Fig. S13(c)), while  $|G(r)|$  and  $|S(r)|$  has an exponential decay with short correlation lengths (Fig. S13(d)). This shows the dominant anisotropic SC pairing correlations. The SC pairing correlation for the b-b bond has much faster decay, and the true nature of the SC phase may require further studies on wider cylinders.

As shown in Fig. S13(b), the phase of the SC pairing correlation for the a-a bond has an oscillation with a period of 2, indicating the pair density wave. When  $J_2$  increases to 0.06, the pairing symmetry becomes consistent with  $d$ -wave pairing (Fig. S14(b)). The SC pairing correlation remains dominant comparing to  $|D(r)|$  and  $|G(r)|$ , as shown

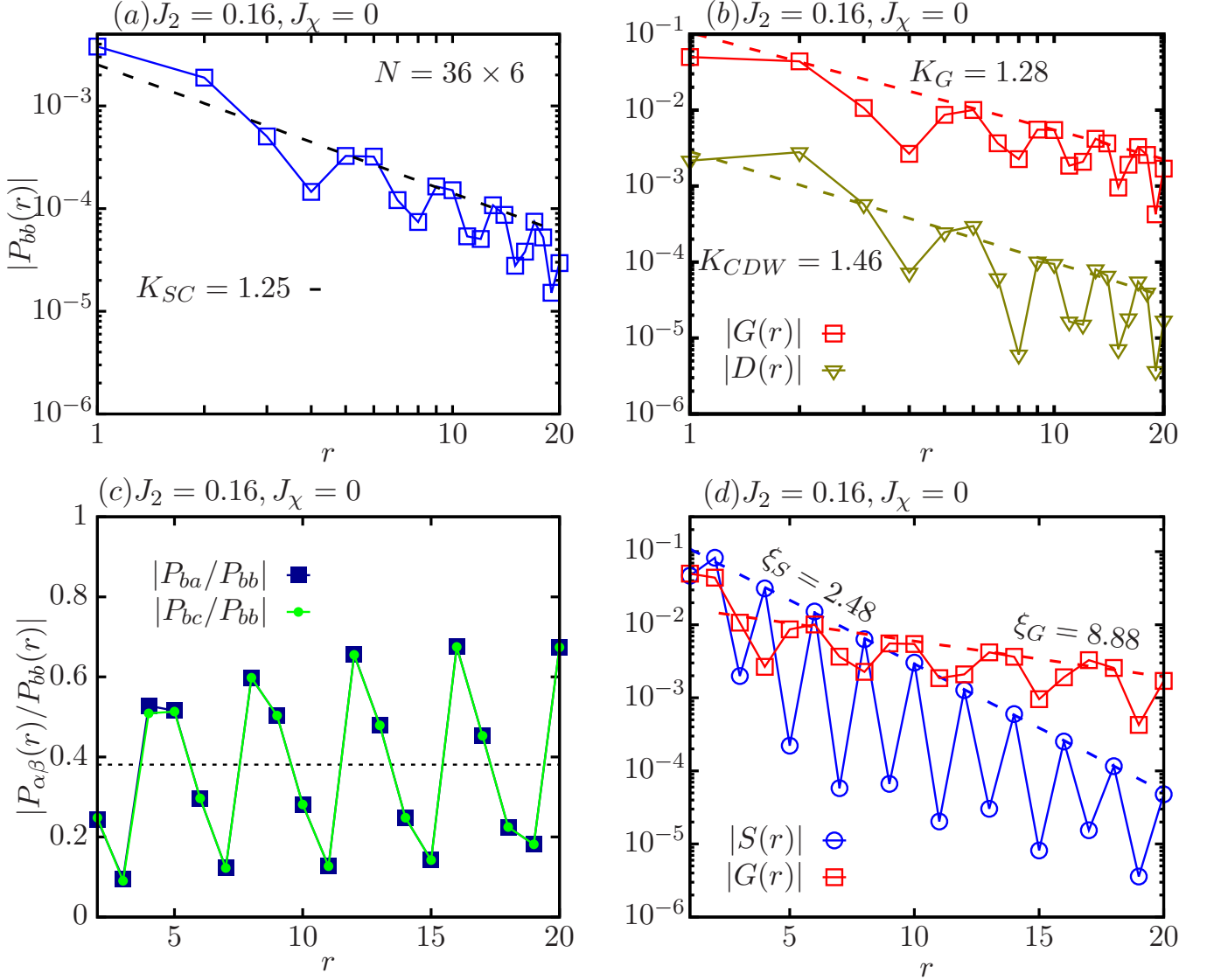


FIG. S9. Various correlations on  $N = 36 \times 6$  system, obtained at  $J_2 = 0.16, J_\chi = 0$ . (a) The SC pairing correlation with bond dimension  $M = 10000$ . The Luttinger exponent is obtained by the straight-line fitting in the log-log plot. (b) The density-density correlation  $|D(r)|$  and single particle correlation  $|G(r)|$ , which are also fit by the power-law relations. (c) The ratio between the magnitudes of SC pairing correlations for different bonds. The dash line indicates the spatial average over distances. (d) The exponential fitting of the spin correlation  $|S(r)|$  and  $|G(r)|$ .

in Figs. S14(c) and (d), respectively. Additionally, the SC pairing correlations for both the a-a and b-b bonds have power-law decaying behaviors with almost the same Luttinger exponents, as shown in Fig. S14(a).

However, a qualitatively different behavior is identified in the long distance for all correlation functions as shown in Figs. S14(a), (c), (d), and (e). Furthermore, a visible change of behavior in the electron density can be seen on the two sides of the system, as shown in Fig. S14(f), suggesting a phase separation that occurs around  $x \approx 29$  separating hole rich region from the spin rich region in the system of  $L_x = 40$ . Future studies are needed to identify the full nature of the phase with larger  $L_y$  which may suppress the phase separation.

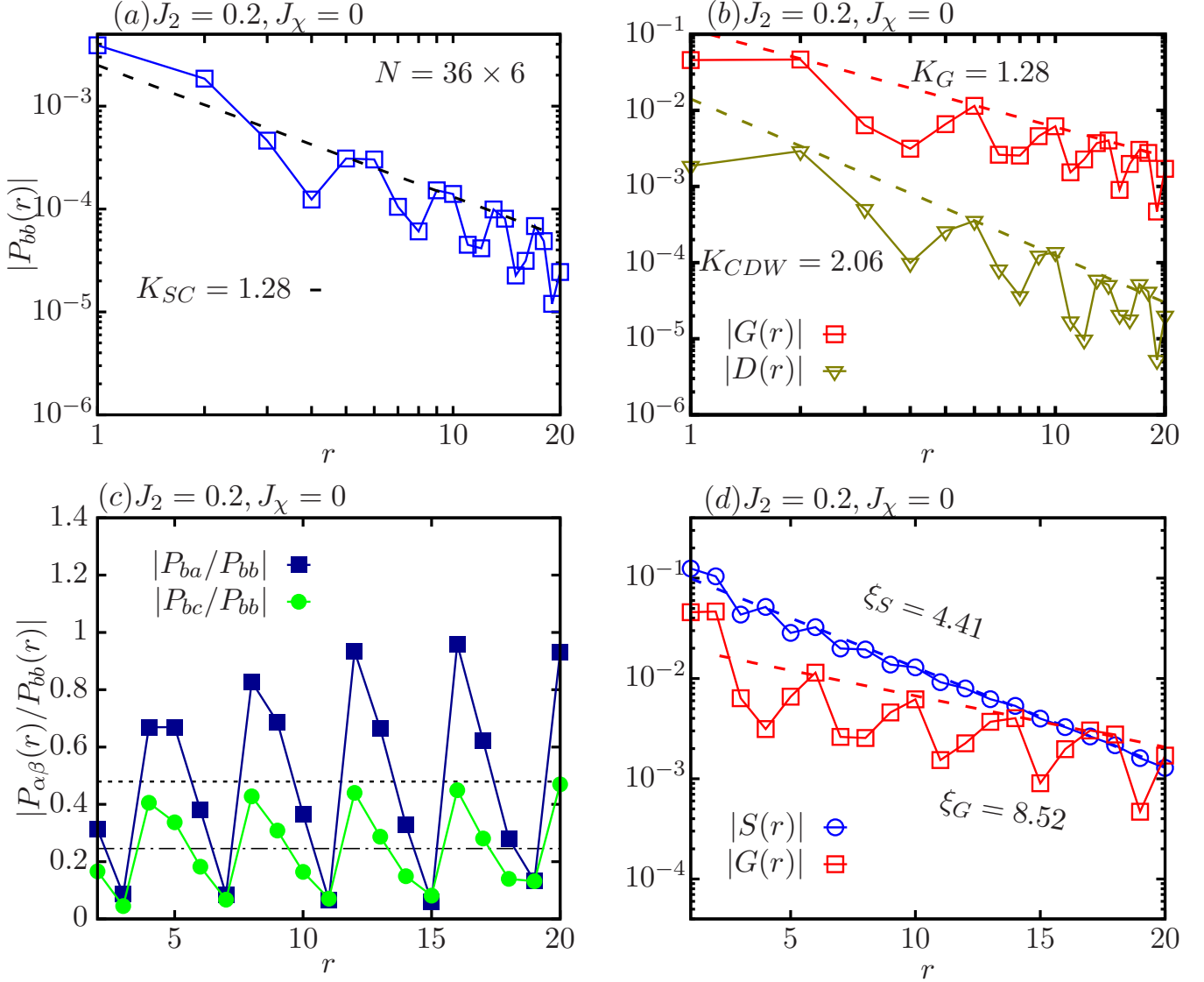


FIG. S10. Various correlations on  $N = 36 \times 6$  system, obtained at  $J_2 = 0.2, J_\chi = 0$ . (a) The SC pairing correlation with bond dimension  $M = 10000$ . The Luttinger exponent is obtained by the straight-line fitting in the log-log plot. (b) The density-density correlation  $|D(r)|$  and single particle correlation  $|G(r)|$ , which are also fit by the power-law relations. (c) The ratio between the magnitudes of SC pairing correlations for different bonds. The dashed line and dashed dotted line indicate the spatial average over distances. (d) The exponential fitting of the spin correlation  $|S(r)|$  and  $|G(r)|$ .

#### iv. FERMI SURFACE EVOLUTION

In Figs. S15(a) - (f) we show the electron occupation number in the momentum space  $N(\mathbf{k}) = \frac{1}{N'} \sum_{i,j,\sigma} \langle \hat{c}_{i,\sigma}^\dagger \hat{c}_{j,\sigma} \rangle e^{i\mathbf{k} \cdot (\mathbf{r}_i - \mathbf{r}_j)}$  with summations over middle  $N' = 12 \times 6$  sites in a  $N = 36 \times 6$  system for different parameters in SC1, SC2, and SC0 phases. For the SC1 phase at small  $J_2$ , hole pockets form around the  $\mathbf{K}$  points, which indicates the hole dynamics in the doped regime may be induced by the  $120^\circ$  AFM fluctuations. It also has a closed Fermi surface around the  $\Gamma = (0, 0)$  point. For the SC2 state at a smaller  $J_2 = 0.05$ , a closed Fermi surface is formed around the  $\Gamma = (0, 0)$  point with near isotropic occupations in the momentum space, which is consistent with the isotropic topological  $d + id$ -wave SC. At larger  $J_2 = 0.1$  and  $0.2$ , a hole pocket appears at  $\mathbf{M}'$  point (which is different from the spin structure peak at  $\mathbf{M}$  points), breaking the  $C_3$  rotational symmetry.

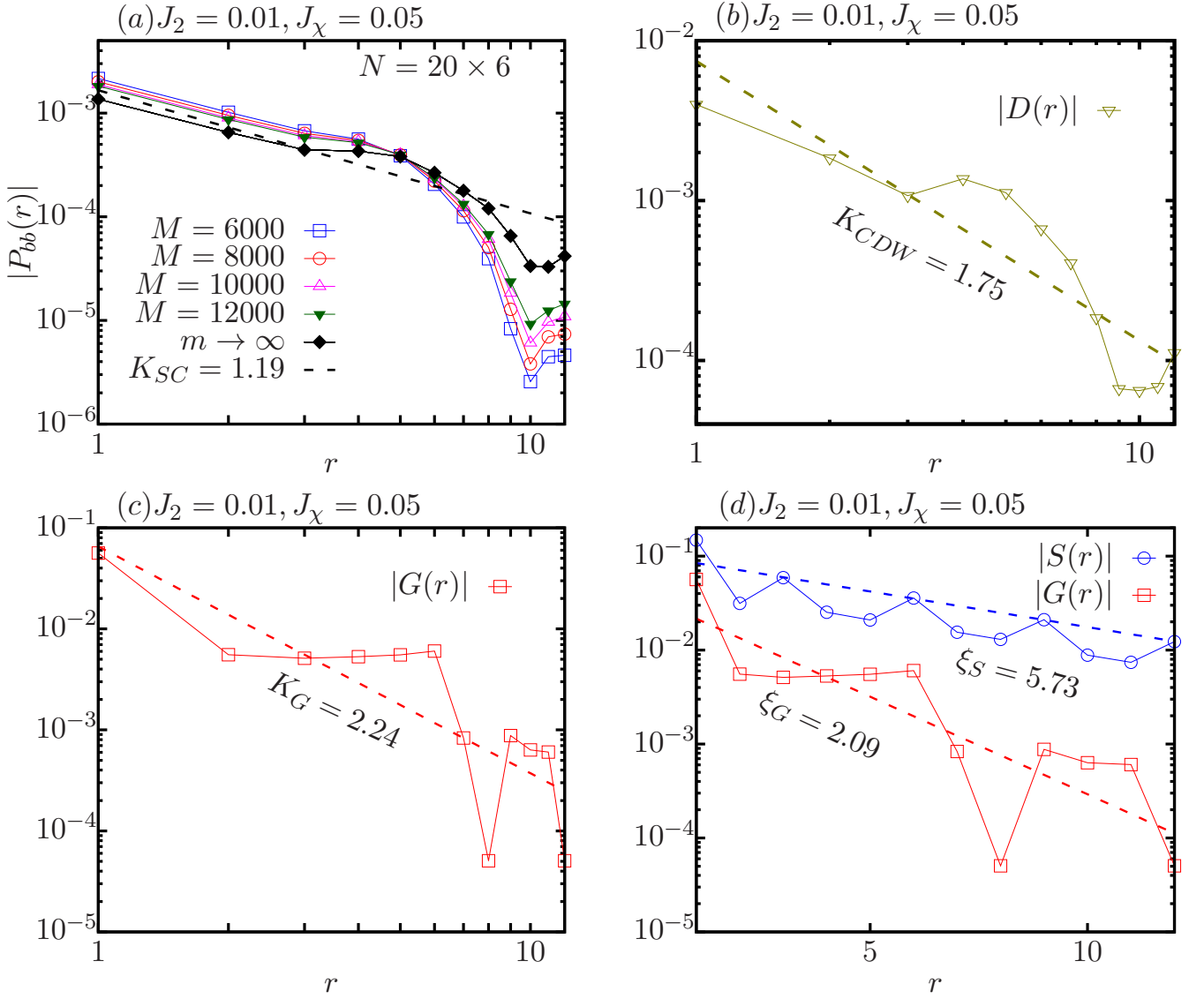


FIG. S11. Various correlations on  $N = 20 \times 6$  system, obtained at  $J_2 = 0.01, J_\chi = 0.05$ . (a) The SC pairing correlation with various bond dimensions. The Luttinger exponent is obtained by the straight-line fitting in the infinite bond dimension limit. (b) The density-density correlation  $|D(r)|$  which is fit by the power-law relation. (c) The single particle correlation  $|G(r)|$  which is also fit by the power-law relation. (d) The exponential fitting of the spin correlation  $|S(r)|$  and  $|G(r)|$ . The reference point is chosen at  $r_0 = (3, 1)$ , and the fitting is for data up to the distance  $L_x/2$ .

## v. ELECTRON DENSITY EVOLUTION

As shown in Figs. S16(a) - (d), a finite electron density oscillation in real space is observed in all states due to the tendency of charge density wave, although the density-density correlations always decay much faster than SC correlations. These results are qualitatively consistent with the behaviors of Luther-Emery liquid.

## vi. NUMERICAL DATA AND PROGRAM CODE AVAILABILITY

The main results of the study are presented within the article and its Supplementary. The digital data and the codes implementing the calculations of this study are available from the corresponding author upon reasonable request.

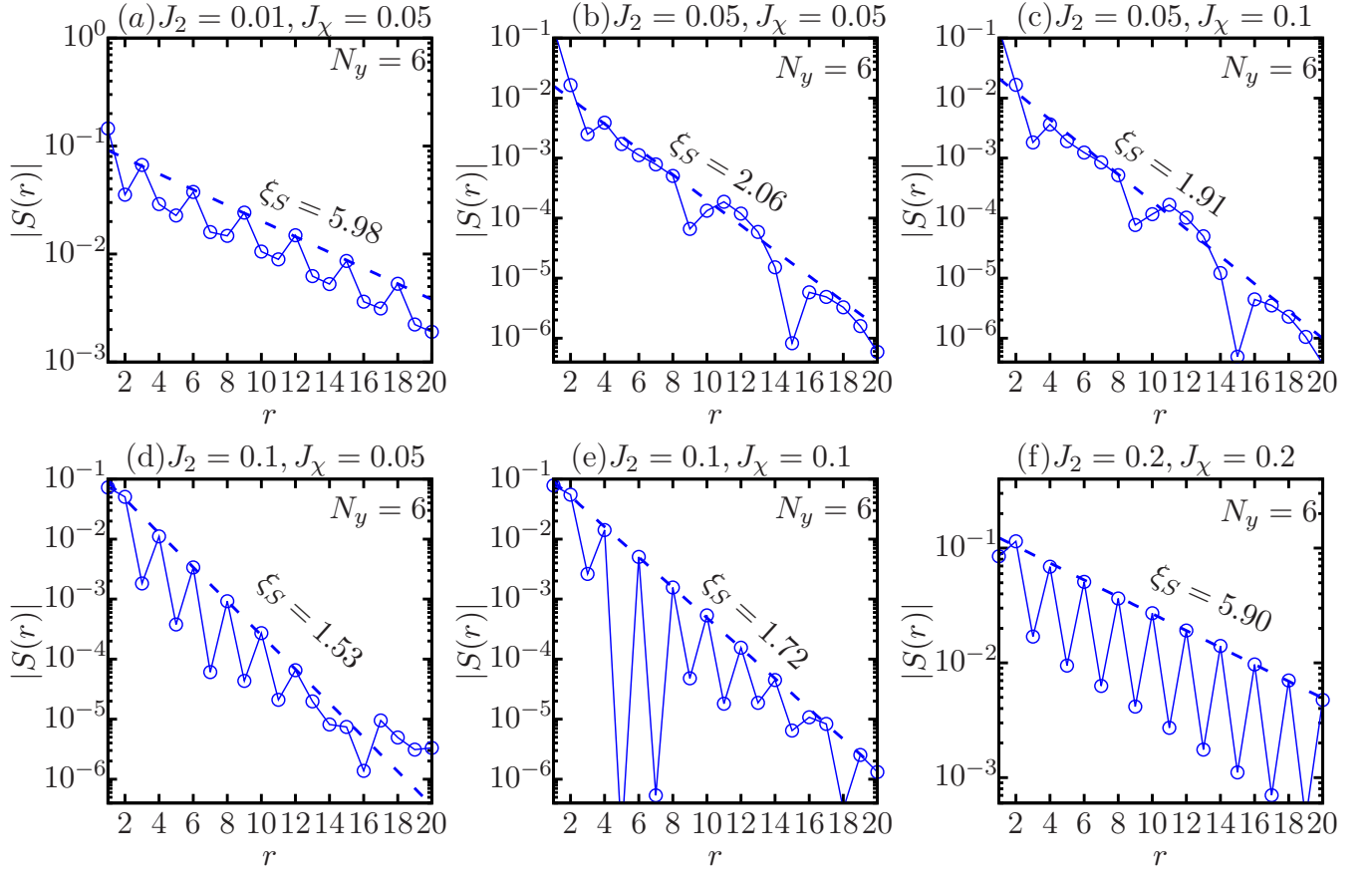


FIG. S12. The spin correlations for (a) SC1 state, (b) - (c) isotropic  $d+id$ -wave TSC states, (d) - (e) nematic  $d+id$ -wave TSC states, and (f) nematic d-wave SC0 state on  $N = 36 \times 6$  system and  $\delta = 1/12$ , obtained at various  $J_2$  and  $J_\chi$  with infinite  $M$  extrapolated data.

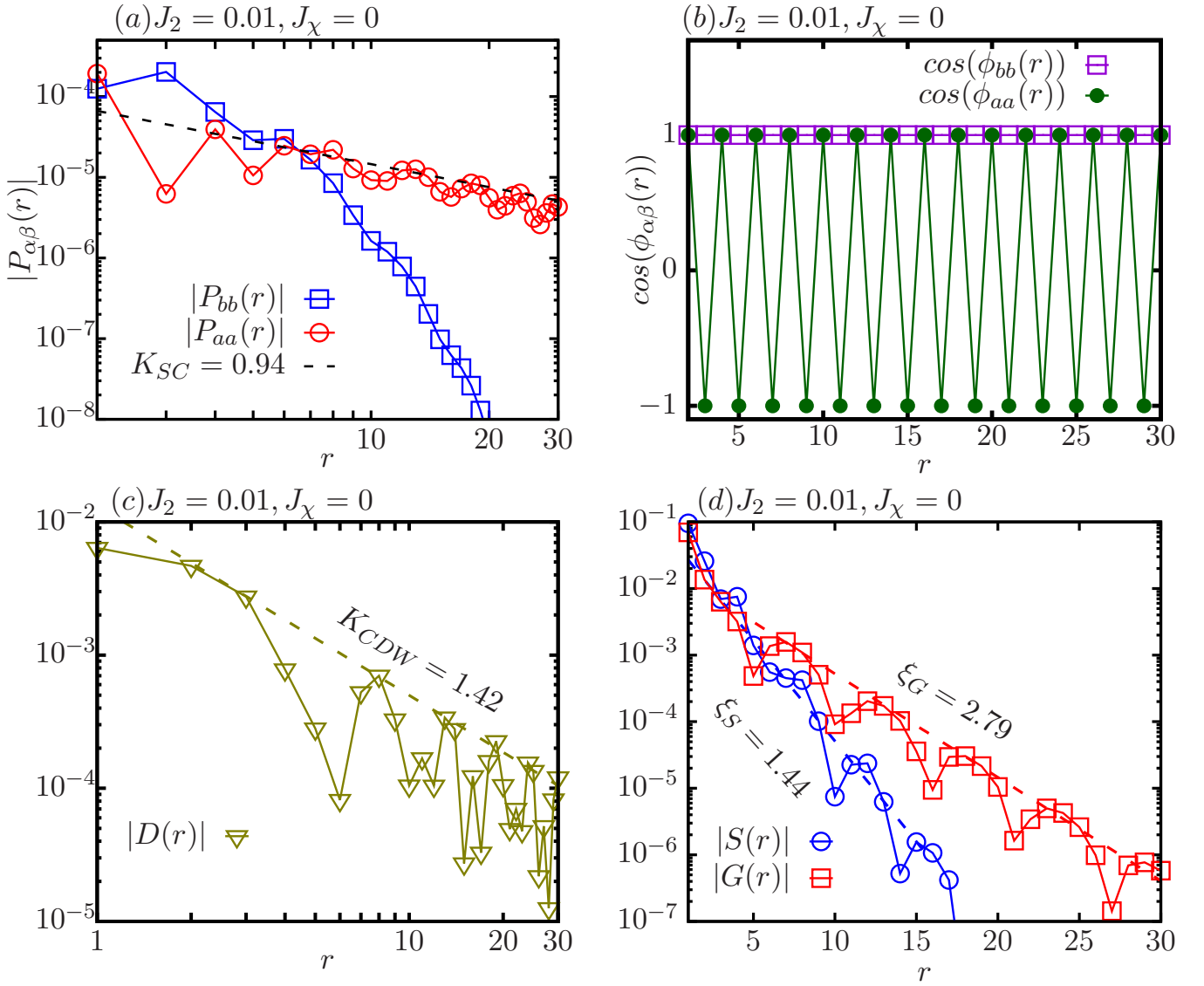


FIG. S13. Various correlations on  $N = 48 \times 4$  system, obtained at  $J_2 = 0.01, J_\chi = 0$ . (a) The SC pairing correlation with bond dimension  $M = 10000$ . The Luttinger exponent is obtained by the straight-line fitting of  $|P_{aa}(r)|$  in the log-log plot. (b) The phases for SC pairing correlations  $\phi_{\alpha\beta}(r)$ . (c) The density-density correlation  $|D(r)|$ , which is also fit by the power-law relation. (d) The exponential fitting of the spin correlation  $|S(r)|$  and single particle correlation  $|G(r)|$ .

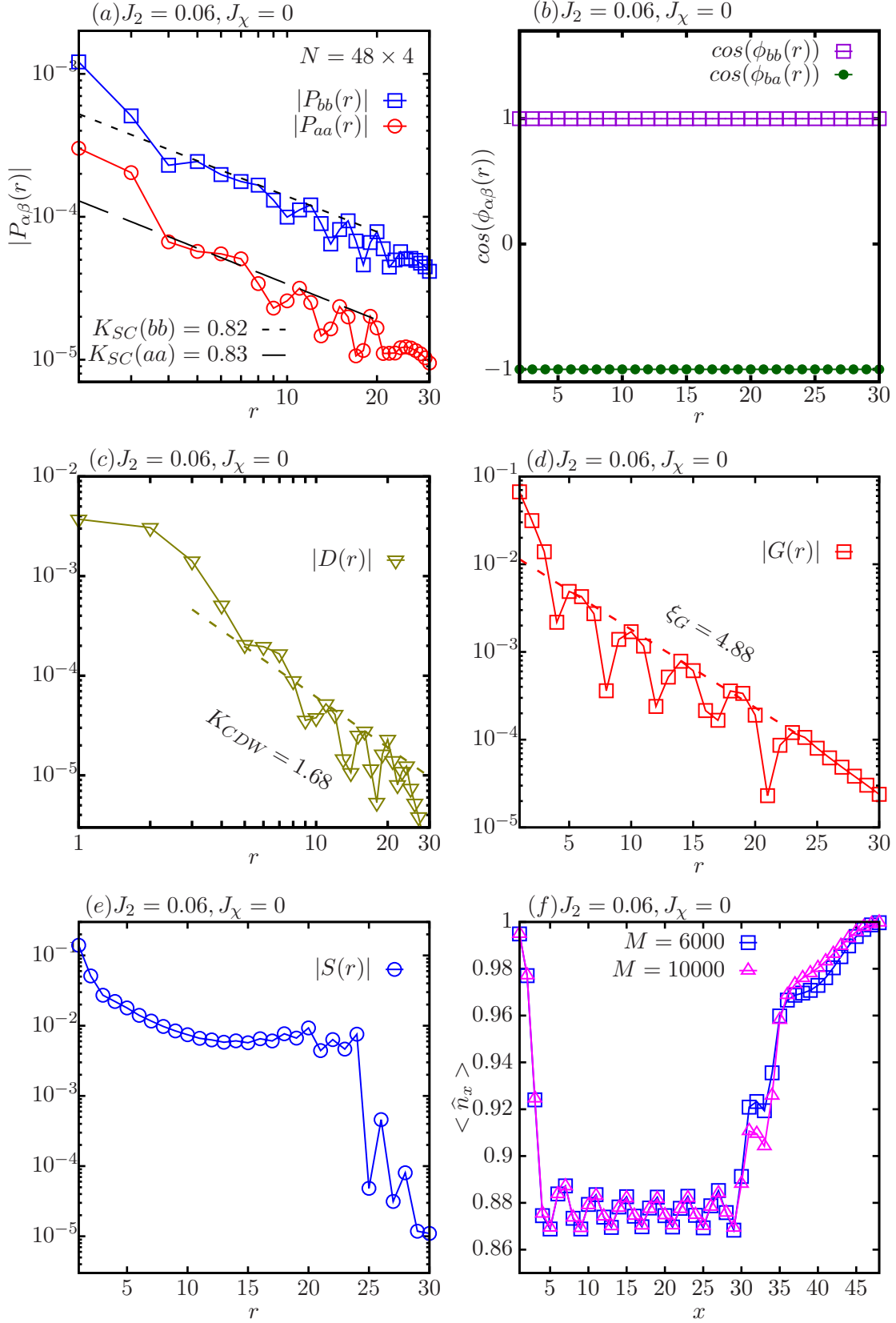


FIG. S14. Various correlations on  $N = 48 \times 4$  system, obtained at  $J_2 = 0.06, J_\chi = 0$ . (a) The SC pairing correlation with bond dimension  $M = 10000$ . The Luttinger exponents are obtained by the straight-line fitting of  $|P_{aa}(r)|$  and  $|P_{bb}(r)|$  in the log-log plot. (b) The phases for SC pairing correlations  $\phi_{\alpha\beta}(r)$ . (c) The density-density correlation  $|D(r)|$ , which is also fit by the power-law relation. (d) The exponential fitting of single particle correlation  $|G(r)|$ . (e) The spin correlation  $|S(r)|$ . (f) The electron density obtained with different  $M$ . All reference points for the correlations are chosen at  $x_0 = 10$

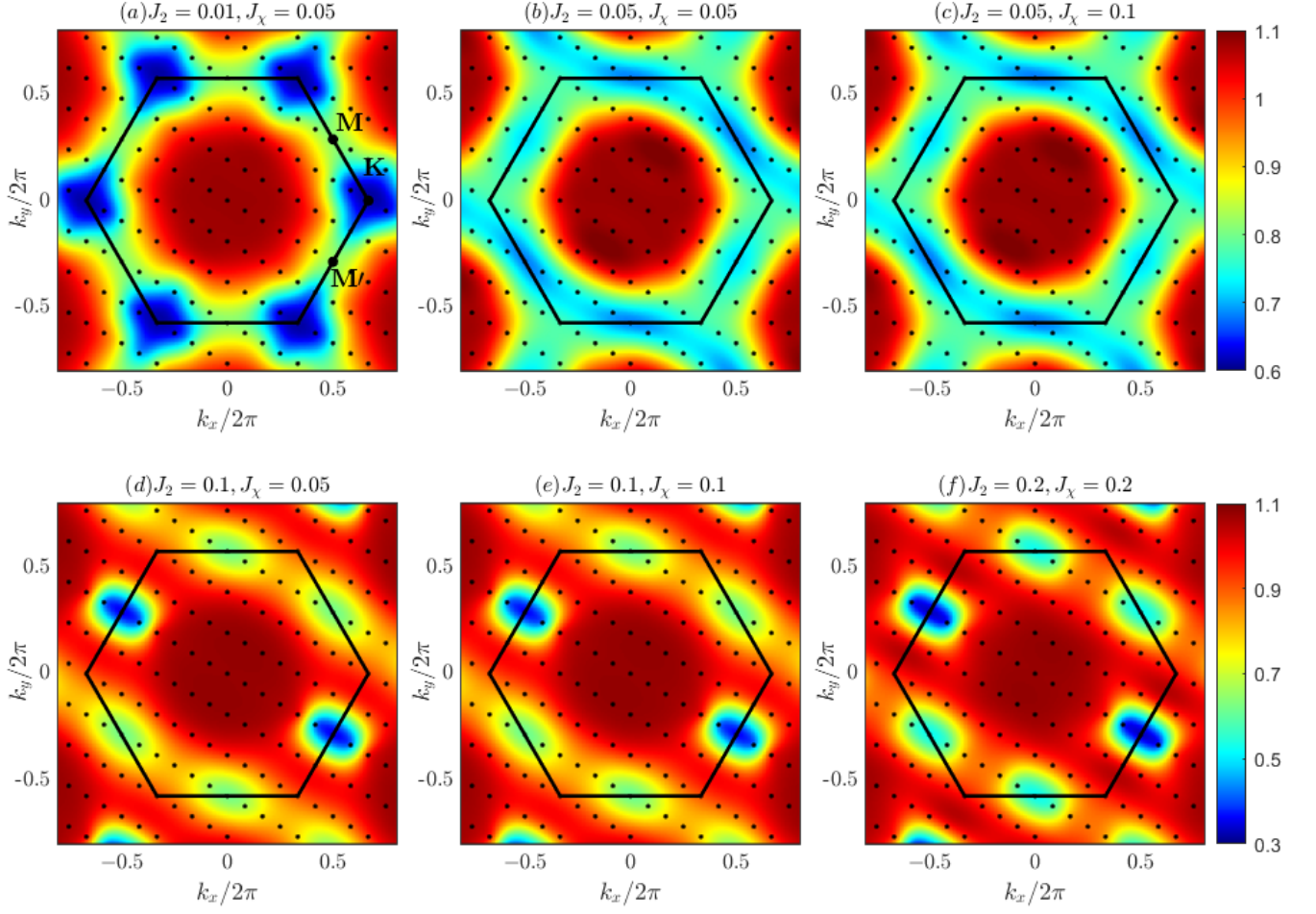


FIG. S15. The electron momentum distribution for (a) SC1 state, (b) - (c) isotropic  $d + id$ -wave TSC states, (d) - (e) nematic  $d + id$ -wave TSC states, and (f) nematic  $d$ -wave SC0 state obtained at various  $J_2$  and  $J_\chi$ . The first Brillouin zone is indicated by the solid line with the  $\mathbf{M}$ ,  $\mathbf{M}'$  and  $\mathbf{K}$  points marked, and the black dots represent the allowed discrete momenta for the finite system with  $N' = 12 \times 6$  sites and  $\delta = 1/12$  with  $M = 10000$ .

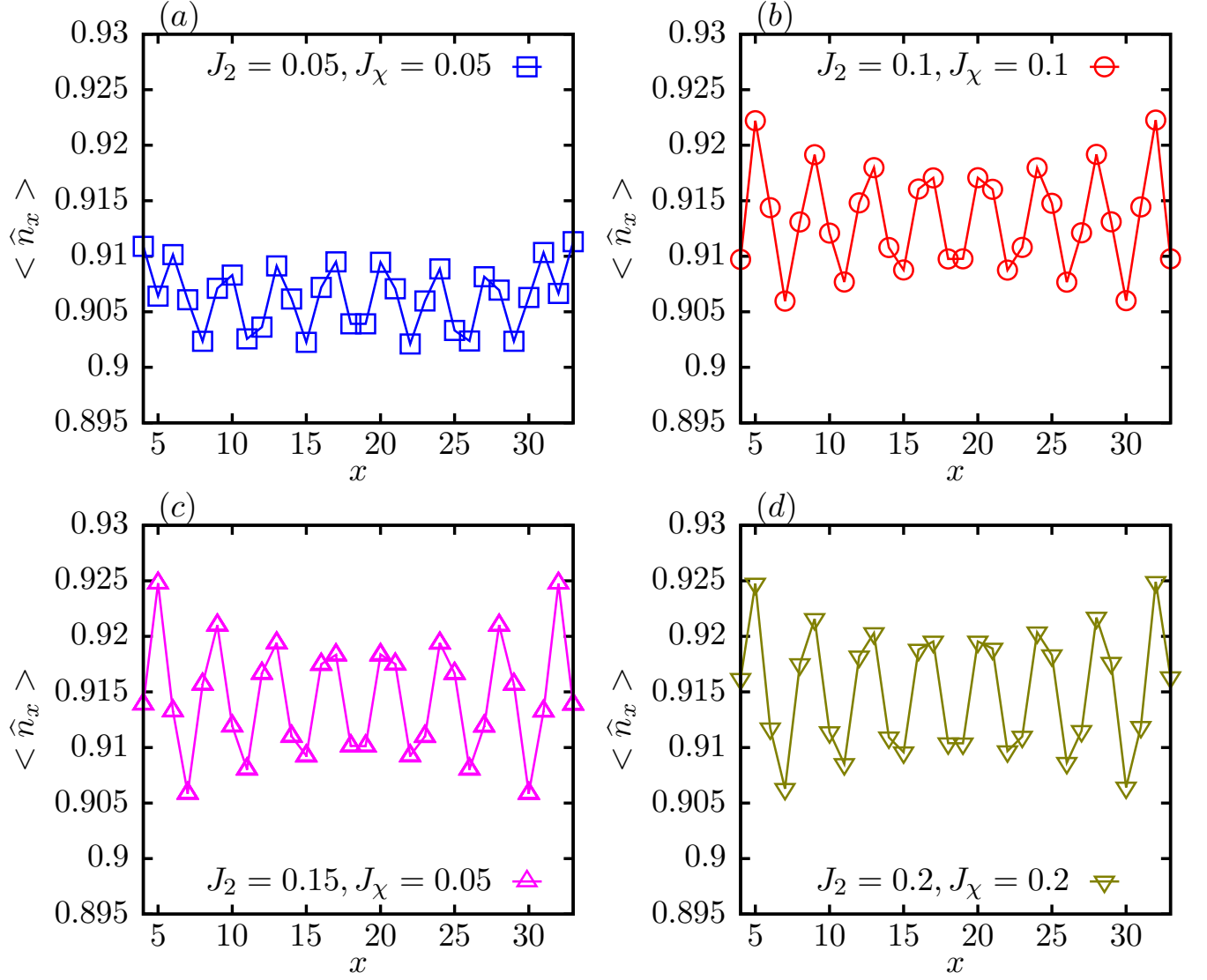


FIG. S16. The electron density for various  $J_2$  and  $J_\chi$ , obtained on  $N = 36 \times 6$  system and  $\delta = 1/12$  with  $M = 10000$ .  $x$  refers to the distance from the left edge in the x-direction.